PTEP

Prog. Theor. Exp. Phys. **2020**, 123D01 (34 pages)
DOI: 10.1093/ptep/ptaa139

An event excess observed in the deeply bound region of the ^{12}C(K^-,p) missing-mass spectrum

Yudai Ichikawa[1,*], Junko Yamagata-Sekihara[2], Jung Keun Ahn[3], Yuya Akazawa[4], Kanae Aoki[4], Elena Botta[5,6], Hiroyuki Ekawa[7], Petr Evtoukhovitch[8], Alessandro Feliciello[5], Manami Fujita[1], Toshiyuki Gogami[9], Shoichi Hasegawa[1], Tomoyuki Hasegawa[10], Shuhei Hayakawa[11,1], Tomonori Hayakawa[11], Satoru Hirenzaki[12], Ryotaro Honda[4], Kenji Hosomi[1], Ken'ichi Imai[1], Wooseung Jung[3], Shunsuke Kanatsuki[9], Shin Hyung Kim[3], Shinji Kinbara[14,1], Kazuya Kobayashi[11], Jaeyong Lee[15], Simonetta Marcello[5,6], Koji Miwa[13], Taejin Moon[15], Tomofumi Nagae[9], Yoshiyuki Nakada[11], Manami Nakagawa[7], Takuya Nanamura[9], Megumi Naruki[9,1], Atsushi Sakaguchi[11], Hiroyuki Sako[1], Susumu Sato[1], Yuki Sasaki[13], Kotaro Shirotori[16], Hitoshi Sugimura[17], Toshiyuki Takahashi[4], Hirokazu Tamura[13,1], Kiyoshi Tanida[1], Zviadi Tsamalaidze[8], Mifuyu Ukai[4,13], and Takeshi O. Yamamoto[1]

[1]*ASRC, Japan Atomic Energy Agency, Ibaraki 319-1195, Japan*
[2]*Department of Physics, Kyoto Sangyo University, Kyoto 603-8555, Japan*
[3]*Department of Physics, Korea University, Seoul 02841, Republic of Korea*
[4]*Institute of Particle and Nuclear Study (IPNS), High Energy Accelerator Research Organization (KEK), Tsukuba, 305-0801, Japan*
[5]*INFN, Istituto Nazionale di Fisica Nucleare, Sez. di Torino, I-10125 Torino, Italy*
[6]*Dipartimento di Fisica, Università di Torino, I-10125 Torino, Italy*
[7]*RIKEN Cluster for Pioneering Research, Wako 351-0198, Japan*
[8]*Joint Institute for Nuclear Research, Dubna, Moscow Region 141980, Russia*
[9]*Department of Physics, Kyoto University, Kyoto 606-8502, Japan*
[10]*Allied Health Sciences, Kitasato University, Sagamihara 252-0373, Japan*
[11]*Department of Physics, Osaka University, Osaka 560-0043, Japan*
[12]*Department of Physics, Nara Women's University, Nara 630-8506, Japan*
[13]*Department of Physics, Tohoku University, Sendai 980-8578, Japan*
[14]*Physics Department, Gifu University, 1-1 Yanagido, Gifu 501-1193, Japan*
[15]*Department of Physics and Astronomy, Seoul National University, Seoul 08826, Republic of Korea*
[16]*Research Center for Nuclear Physics (RCNP), Osaka University, Osaka 567-0047, Japan*
[17]*Accelerator Laboratory, High Energy Accelerator Research Organization (KEK), Tsukuba, 305-0801, Japan*
*E-mail: yudai@post.j-parc.jp

Received May 28, 2020; Revised September 8, 2020; Accepted September 8, 2020; Published December 18, 2020

We have measured, for the first time, the inclusive missing-mass spectrum of the ^{12}C(K^-,p) reaction at an incident kaon momentum of 1.8 GeV/c at the J-PARC K1.8 beamline. We observed a prominent quasi-elastic peak ($K^-p \to K^-p$) in this spectrum. In the quasi-elastic peak region, the effect of secondary interaction is apparently observed as a peak shift, and the peak exhibits a tail in the bound region. We compared the spectrum with a theoretical calculation based on the Green's function method by assuming different values of the parameters for the $\bar{K}$–nucleus optical potential. We found that the spectrum shape in the binding-energy region $-300\,\mathrm{MeV} < B_K < 40\,\mathrm{MeV}$ is best reproduced with the potential depths $V_0 = -80\,\mathrm{MeV}$ (real part) and $W_0 = -40\,\mathrm{MeV}$ (imaginary part). On the other hand, we observed a significant event excess in the deeply bound region around $B_K \sim 100\,\mathrm{MeV}$, where the major decay channel of $K^-NN \to \pi\Sigma N$ is energetically closed, and the non-mesonic decay modes ($K^-NN \to \Lambda N$ and ΣN) should mainly contribute. The enhancement is fitted well by a Breit–Wigner function with

a kaon-binding energy of 90 MeV and width 100 MeV. A possible interpretation is a deeply bound state of a Y^*-nucleus system.

Subject Index D33

1. Introduction

One of the directions of nuclear physics research is to extend the concept of nuclei as nucleon many-body systems into that of hadron many-body systems. The study of hypernuclei is a well-known example of this extension; hyperons in nuclei provide us with new means to deepen our understanding of nuclear force and structure. Here we discuss a new type of extension, meson–baryon many-body systems called mesonic nuclei, where mesons exist in a nucleus as real particles. Some types of mesonic nuclei are predicted theoretically; however, the experimental results are limited. Specifically, physicists have shown much interest in kaonic nuclei, quasi-bound states between a $\bar{K}$ and nuclei. This is due to the fact that the $\bar{K}N$ interaction has a strong attraction in the isospin $I = 0$ channel, and thus should form a bound state. However, the depth of the $\bar{K}$–nucleus potential is a long-standing puzzle and is key to studying the kaonic nuclei.

Kishimoto suggested the existence of kaonic nuclei with a medium atomic number based on the strong attraction in the $\bar{K}N$ system in 1999 [1]. Then, Akaishi and Yamazaki discussed the possibility of kaonic nuclei in few-body systems in 2002 [2], in which the large binding energy could make the decay width narrow. Since then, kaonic nuclei has been actively investigated, both theoretically and experimentally.

Specifically, the simplest kaonic nucleus, called K^-pp, a quasi-bound state of a $\bar{K}$ and two nucleons with isospin $I = 1/2$ and spin parity $J^P = 0^-$, has attracted much attention. K^-pp has also been studied theoretically using different approaches to $\bar{K}N$ interaction and few-body calculation methods [3].

Recently, some exotic hadrons have been reported, such as pentaquark particles [4,5]. Their structures, however, are not yet well established. In this discussion about kaonic nuclei, the structure of $\Lambda(1405)$ is critical [6,7]. Whether it is an excited state of a Λ hyperon with three (uds) constituent quarks or a $\bar{K}N$ molecular state has been a long-standing puzzle in hadron spectroscopy. A lattice QCD calculation favors the molecular picture of $\bar{K}$ and N [8].

The first experimental result on K^-pp was reported by the FINUDA Collaboration [9]. They used the stopped K^- absorption reaction on ^{6,7}Li and ^{12}C targets and found a bump structure in the Λp invariant-mass spectrum. The obtained binding energy and decay width were $115\,^{+6}_{-5}\,(\text{stat.})\,^{+3}_{-4}\,(\text{syst.})$ MeV and $67\,^{+14}_{-11}\,(\text{stat.})\,^{+2}_{-3}\,(\text{syst.})$ MeV, respectively. The DISTO Collaboration also reported a possible signal of K^-pp by using the $pp \to K^+\Lambda p$ reaction at $T_p = 2.85$ GeV [10]. They obtained a binding energy of $103 \pm 3\,(\text{stat.}) \pm 5\,(\text{syst.})$ MeV and a decay width of $118 \pm 8\,(\text{stat.}) \pm 10\,(\text{syst.})$ MeV. Furthermore, the DISTO Collaboration also reported that there was no signal at $T_p = 2.5$ GeV. The HADES Collaboration measured the same $pp \to K^+\Lambda p$ reaction at 3.5 GeV and found no signal [11]. Finally, no peak was observed in the inclusive spectrum of the $d(\gamma, K^+\pi^-)X$ reaction at $E_\gamma = 1.5$–2.4 GeV at LEPS [12].

J-PARC has also contributed to the search for the kaonic nuclei. The E15 and E27 experiments were conducted to search for the K^-pp at K1.8 BR and K1.8 beamline, respectively. The E27 Collaboration used the $d(\pi^+, K^+)\Sigma^0 p$ reaction at $p_{\pi^+} = 1.69$ GeV/c and observed a broad bump

structure [13]. The deduced binding energy and decay width were $95\,^{+18}_{-17}\,(\text{stat.})\,^{+30}_{-27}\,(\text{syst.})$ MeV and $162\,^{+87}_{-45}\,(\text{stat.})\,^{+66}_{-78}\,(\text{syst.})$ MeV, respectively. The E15 Collaboration found a distinct peak structure in the Λp invariant mass of the $^3\text{He}(K^-, \Lambda p)n$ reaction at 1.0 GeV/c [14]. The binding energy and the decay width of the Breit–Wigner form were $47 \pm 3\,(\text{stat.})\,^{+3}_{-6}\,(\text{syst.})$ MeV and $115 \pm 7\,(\text{stat.})\,^{+10}_{-20}\,(\text{syst.})$ MeV, respectively. Moreover, the parameter of the s-wave Gaussian reaction form factor was also evaluated as $Q_0 = 381 \pm 14\,(\text{stat.})\,^{+57}_{-0}\,(\text{syst.})$ MeV. The production cross section was estimated as $\sigma_{Kpp} \times Br_{\Lambda p} = 11.8 \pm 0.4\,(\text{stat.})\,^{+0.2}_{-1.7}\,(\text{syst.})\,\mu$b, which is approximately 10^{-3} when related to the cross section of K^-p quasi-elastic scattering.

Let us suppose there exists a K^-pp bound state with a binding energy $\gtrsim$ 50 MeV. Then, it is reasonable to expect the existence of heavier kaonic nuclei. The $\bar{K}$–nucleus potentials for heavier systems were developed with systematic data samples of kaonic atom X-rays. Even though the SIDDHARTA data on the kaonic hydrogen X-rays strongly constrained the potential strength [15], two sets of parameters, "shallow" and "deep," are proposed; both sets reproduce the data reasonably well.

A "shallow" potential, where the real part of the potential depth is in the range $-80\,\text{MeV} \lesssim V_0 \lesssim -40\,\text{MeV}$, is obtained with a simple $t\rho$ approach [16] and the SU(3) chiral unitary model [17–20]. The shallowest potential is derived by further requiring self-consistency [19,20].

In contrast, a "deep" potential ($-200\,\text{MeV} \lesssim V_0 \lesssim -150\,\text{MeV}$) usually gives a better χ^2 in the fit. The main difference between the "deep" and "shallow" potentials is the nonlinear density terms (ρ). For example, $b\rho + B\rho^2/\rho_0$ terms, where b and B are fitting parameters, are introduced considering the multi-nucleon absorptive and dispersive contributions [16]. Also, a $t\rho$ approach with a multiplicative function [21] and the Fourier–Bessel method [22] predicts such "deep" potentials. Similarly, Ref. [23] gives a "deep" potential. This study introduces a single-nucleon density-dependent potential $V^{(1)}_{\bar{K}}(\rho)$, generated by the Ikeda–Hyodo–Weise amplitude [24], and a phenomenological density-dependent potential $V^{(2)}_{\bar{K}}(\rho)$ to represent the multi-nucleon absorptive and dispersive processes.

Notably, the origin of the nonlinear terms in density is multi-nucleon absorptions. In the stopped K^- reactions, the fraction of non-mesonic absorption by multi-nucleons amounts to approximately 20% in a wide mass number range [25]. However, no microscopic studies existed until recent years, and no quantitative analyses of the $\bar{K}N$ potentials have considered multi-nucleon absorptions. Therefore, the widths resulting from multi-nucleon absorption processes are not well understood. Note that most of the experimental observations suggesting the existence of K^-pp bound states claim a large width, $\geq$ 100 MeV, greater than the decay width of $\Lambda(1405)$. There should be sizable non-mesonic decay-widths of the order of 100 MeV.

In the experimental investigations of heavier kaonic nuclei, the KEK E548 experiment was conducted to measure both $^{12}\text{C}(K^-, n)$ and $^{12}\text{C}(K^-, p)$ spectra [26]. They found that the potential depths $V_0 + iW_0 \sim -190 - 40i$ MeV and $V_0 + iW_0 \sim -160 - 50i$ MeV reproduced well the $^{12}\text{C}(K^-, n)$ and $^{12}\text{C}(K^-, p)$ spectra, respectively. However, their spectra cannot be compared with theoretical inclusive spectra [27]. Their measurement required the coincidence of one charged particle near the target system and the spectra would be deformed because of this bias.

This measurement is similar to that of KEK E548. We have measured the inclusive missing mass spectrum of the $^{12}\text{C}(K^-, p)$ reaction at $p_{K^-} = 1.8$ GeV/c at the J-PARC K1.8 beamline. In these conditions, the momentum of the outgoing protons from kaonic nucleus production is considered to be approximately 2.2 GeV/c at a very forward angle of $\theta_p < 5°$. The most important advantage to measuring the outgoing proton at a very forward angle is that momentum transfer in the $K^-p \to K^-p$

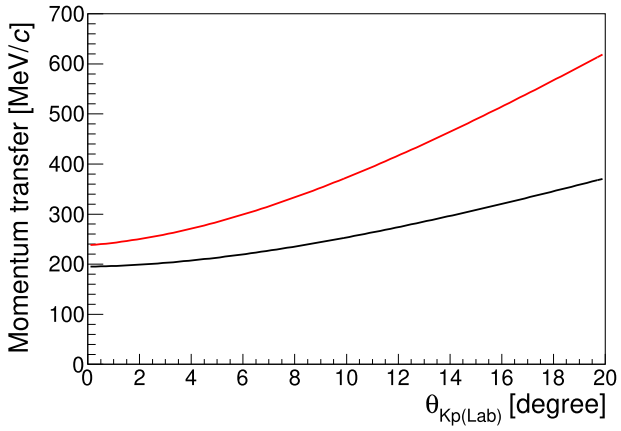

Fig. 1. Momentum transfer of the $K^- p \to K^- p$ elastic scattering as a function of the scattering angle θ_{Kp} in the laboratory system. The red and black lines show the situations at $p_{K^-} = 1.8\,\mathrm{GeV}/c$ for J-PARC E05 and $1.0\,\mathrm{GeV}/c$ for KEK E548, respectively.

elastic scattering is low ($\lesssim 300\,\mathrm{MeV}/c$; Fig. 1), comparable with the Fermi motion in ^{12}C. A critical difference from KEK E548 is that we require an outgoing proton in the forward direction to measure an inclusive spectrum. Another difference is the momentum of the incident kaon. For KEK E548, it was $1.0\,\mathrm{GeV}/c$, whereas it is $1.8\,\mathrm{GeV}/c$ in this measurement. The kaon elastic-scattering cross section has a maximum at $1.0\,\mathrm{GeV}/c$, and it decreases monotonically to $1.8\,\mathrm{GeV}/c$. The maximum is because of an s-channel resonance. While the incident beam momenta are different, the momentum transfer in the $K^- p \to K^- p$ elastic scattering at very forward angles for each incident momentum is similar. Therefore, the difference in the missing-mass spectrum for each incident beam momentum should be small. A further difference is the missing-mass resolution of the detector system. It is 4.2 MeV in σ, which is a significant improvement regarding the 10 MeV in KEK E548. By considering the large widths generally observed for the $K^- pp$, this missing-mass resolution would be enough to observe the peak structure.

2. Experimental setup

This measurement was conducted as part of the J-PARC E05 pilot run, searching for a Ξ-hypernucleus by using the $^{12}\mathrm{C}(K^-, K^+)$ reaction. The pilot run was conducted at the K1.8 beamline of the J-PARC hadron experimental facility from 26 October to 19 November, 2015.

A carbon graphite target of $9.364\,\mathrm{g\,cm^{-2}}$ thickness was irradiated with 84.9×10^9 K^- of $1.8\,\mathrm{GeV}/c$ momentum.[1] Furthermore, we collected data on the $9.538\,\mathrm{g\,cm^{-2}}$-thick polyethylene $[(C_2H_4)_n]$ target at 1.5, 1.6, 1.7, 1.8, and $1.9\,\mathrm{GeV}/c$ K^- beam momenta to evaluate the elementary cross sections. In this paper we focus on the data at $1.8\,\mathrm{GeV}/c$. The results obtained using the other momenta will be reported elsewhere. For calibration, beam pass-through data were also taken with and without the targets at 1.1, 1.2, 1.35, 1.5, and $1.8\,\mathrm{GeV}/c$ using the K^+ beam and 1.2, 1.35, 1.5, 1.8, and $2.0\,\mathrm{GeV}/c$ using the K^- beam, respectively. The typical K^- beam intensity was approximately 6×10^5 per accelerator cycle of 5.5 s with a typical K^-/π^- ratio of approximately 0.8 and a beam spill length of approximately 2 s.

[1] This beam momentum was chosen by considering the maximum elementary cross section of the $p(K^-, K^+)\Xi^-$ reaction to search for the Ξ-hypernucleus.

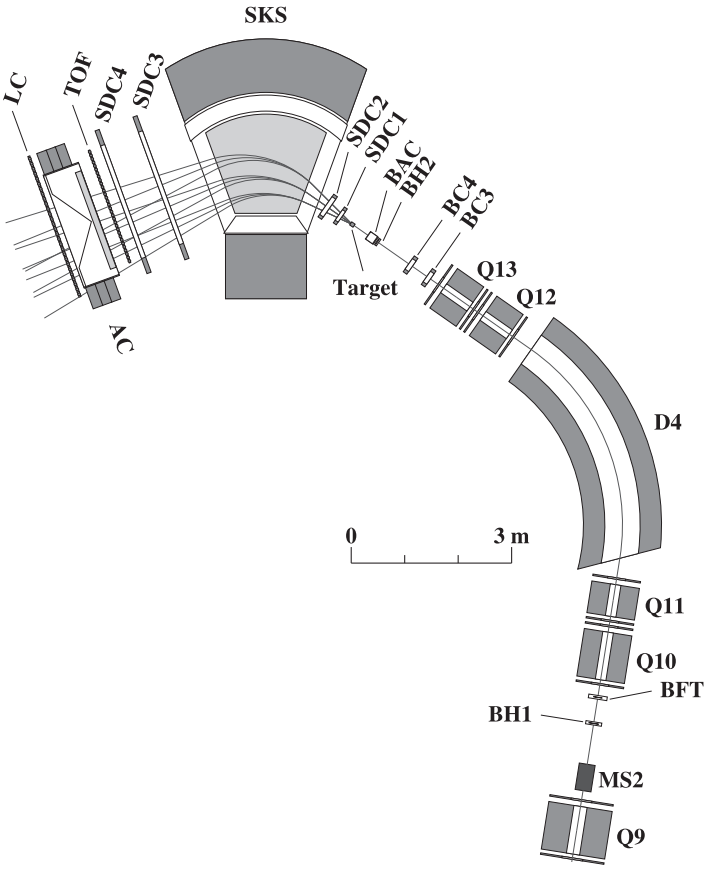

Fig. 2. Schematic view of the experimental setup.

Figure 2 shows a schematic view of the experimental setup. The incident K^- beam was analyzed using a magnetic spectrometer, the K1.8 beamline spectrometer [28]. The outgoing particles, such as K^+, and protons were measured by the Superconducting Kaon Spectrometer (SKS) [28] in the spectrometer configuration called SksMinus [29]. We set the SKS magnetic field at 2.49 T to analyze outgoing K^+ from the Ξ-hypernucleus production with a momentum of approximately 1.4 GeV/c and scattering angle of $\theta_{K^+} < 14°$. SKS has a large angular (∼100 msr) and momentum (1.1–2.4 GeV/c for this measurement) acceptance. Therefore, we could also measure the outgoing protons from the kaonic nucleus production with a momentum of approximately 2.2 GeV/c and scattering angle of $\theta_p < 5°$ at the same time. This section describes details of the experimental setup.

2.1. K1.8 beamline spectrometer

The secondary K^- beam was produced on the primary target (Au, 66 mm thick) by a 30 GeV primary proton beam and delivered to the experimental area via the K1.8 beamline. The K1.8 beamline was designed to provide separated secondary particles with momenta up to 2 GeV/c by using double electrostatic separators (ESS1 and ESS2). The beam was analyzed in the beam analysis section called the K1.8 beamline spectrometer. It consists of two timing plastic scintillation hodoscopes (BH1 and BH2), a tracking detector made of scintillating fibers (BFT), a series of *QQDQQ* magnets (Q10, Q11, D4, Q12, and Q13), two sets of multi-wire drift chambers (BC3 and BC4), and two sets of aerogel Čerenkov counters (BAC1 and BAC2).

BH1 and BH2 are plastic scintillation counters segmented into 11 and 5 modules, respectively. Phototubes (HAMAMATSU H6524MOD) equipped with a three-stage booster were connected to both ends of the BH1 scintillators. For BH2, the same types of phototubes were coupled to the bottom end only. These hodoscopes were used to generate trigger signals and as time-of-flight counters for beam particles, with a typical time resolution of approximately 0.2 ns. BH2 provided reference timing for all the other detectors.

BFT is a tracking detector made of 1 mm-diameter scintillating fibers installed at the upstream part of the *QQDQQ* system [30]. A multi-pixel photon counter device (MPPC) detected the scintillation light from each BFT fiber, and BFT measured the horizontal position of the beam trajectories with a sensitive area of $160^{\mathrm{H}} \times 80^{\mathrm{V}}$ mm^2. It consisted of two layers staggered by 0.5 mm and attained a root-mean-square (rms) spatial resolution of approximately 0.2 mm.

BC3 and BC4 are multi-wire drift chambers with 1.5 mm drift length installed at the exit of the last Q magnet (Q13); they have a six-layer ($xx'uu'vv'$) configuration, where the x-plane measures the horizontal hit position. The wires in the u- and v-planes are tilted by $\pm 15^\circ$ relative to those in the x-plane. The typical rms spatial resolution of both BC3 and BC4 is approximately 0.2 mm. The momenta of beam particles are reconstructed from the track information of BFT, BC3, and BC4 using the third-order transfer matrix through the *QQDQQ* system. The design full width at half maximum (FWHM) value of the momentum resolution is 3.3×10^{-4} [28].

BAC1 and BAC2 are threshold-type silica aerogel Čerenkov counters with a refractive index of $n = 1.03$, corresponding to a threshold momentum of 0.6 GeV/c for pions and 2.0 GeV/c for kaons. These detectors were installed downstream of BH2. Three fine-mesh-type photomultiplier tubes (PMTs; H6614-70UV) were connected to the radiator for each BAC. The analog signals from the PMTs were summed before the discriminators to improve the K/π separation power. The K^- beam detection efficiency is estimated to be approximately 95%, including the inefficiency due to the in-flight decay between BH1 and the BACs. The pion detection efficiency for each BAC is evaluated to be more than 99%. The trigger logic to select the K^- beam was defined as

$$\mathrm{BEAM} \equiv \mathrm{BH2} \times \overline{\mathrm{BAC1} \parallel \mathrm{BAC2}}. \tag{1}$$

2.2. *Superconducting kaon spectrometer (SKS)*

The SKS consists of four sets of multi-wire drift chambers (SDC1, SDC2, SDC3, and SDC4), a superconducting dipole magnet (SKS magnet), a timing plastic scintillator hodoscope (TOF), and two threshold-type Čerenkov counters (AC and LC). It achieves both a good momentum resolution of 3.5×10^{-3} (FWHM) at $p = 2.0$ GeV/c and a large momentum acceptance (1.1–2.4 GeV/c). In this measurement at 1.8 GeV/c, we set the SKS magnetic field to 2.49 T.

SDC1 and SDC2 were installed at the entrance of the SKS magnet with ($xx'vv'uu'$) and ($uu'xx'$) layer configurations, respectively, and a drift length of 2.5 mm. The wires in the u and v planes are tilted by $\pm 15^\circ$ as in BC3 and BC4. The typical rms spatial resolutions are approximately 0.2 mm (SDC1) and 0.15 mm (SDC2). SDC3 and SDC4, which cover a large total area of $2140^{\mathrm{H}} \times 1140^{\mathrm{V}}$ mm^2, were placed at the exit of the SKS magnet. SDC3 and SDC4 have identical structures and the same layer configuration ($xuvxuv$), where the u and v wires are tilted by $\pm 30^\circ$ relative to the x wires. The drift length is 10 mm and the typical rms spatial resolution is approximately 0.25 mm. The outgoing proton's momentum is reconstructed from the hit information on these drift chambers and a calculated field map by using the Runge–Kutta method.

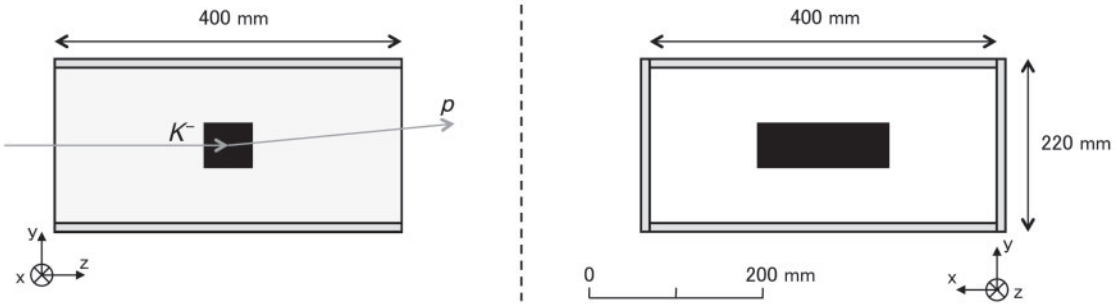

Fig. 3. Schematic view of KIC. The four segments of the KIC counters are indicated by gray boxes.

TOF is a set of plastic counters horizontally segmented into 32 slabs and installed downstream of SDC4. Phototubes (H1949) detect the signal of each segment on both the top and bottom sides. The outgoing proton is identified by the time of flight between BH2 and TOF, along with the flight path length for each track.

AC is a threshold-type silica aerogel ($n = 1.05$) Čerenkov counter for pion veto at the trigger level. Outgoing pions were rejected with a threshold of 0.45 GeV/c. AC was placed just behind TOF, and 5 in phototubes (H-R1584 and Burle-8854) were used for signal detection.

LC is a Lucite Čerenkov counter installed immediately downstream of AC to separate low-momentum protons from pions and kaons at the trigger level. It was segmented into 28 elements of a Lucite (acrylic) radiator with a refractive index of $n = 1.49$, corresponding to a threshold momentum of approximately 0.9 GeV/c for protons. The momentum dependence of the proton detection efficiency is evaluated by using BH2 $\times$ TOF trigger data and is corrected for on a per-event basis. We find that the proton detection efficiency reaches a plateau ($\epsilon_{\mathrm{LC}} \sim 98\%$) at $p_{\mathrm{proton}} = 1.6\,\mathrm{GeV}/c$.

The main trigger of the E05 experiment, called the (K^-, K^+) trigger, was defined as

$$\mathrm{KK} \equiv \mathrm{BEAM} \times \mathrm{TOF} \times \overline{\mathrm{AC}} \times \mathrm{LC} \times \mathrm{MT}. \tag{2}$$

Here, MT is a matrix coincidence trigger considering a hit-segment combination of TOF with LC. It distinguished reaction events at the target from fake triggers originating from the beam hitting the magnet yoke. Since an LC hit was required in the (K^-, K^+) trigger, outgoing protons with low momenta were suppressed at the trigger level. However, outgoing protons in the region of interest have a high momentum of approximately 2.0 GeV/c and LC cannot suppress them. Therefore, the (K^-, p) reaction data were also collected using the (K^-, K^+) trigger. A detection efficiency correction for LC is applied for each event according to the momentum of the outgoing protons in the offline analysis.

2.3. Decay counter KIC

We additionally installed four segments (up, down, left, and right) of plastic scintillation counters, called KIC, surrounding the target to detect decay particles from kaonic nuclei (Fig. 3). Here, the carbon graphite target is shown by a black box, with the z-coordinate corresponding to the beam direction. The gray boxes show the four segments of KIC counters.

KIC was installed to examine the possible distortion effect because of the requirement for at least one charged particle hit in KEK E548. The size of the up and down segments was $400 \times 400\,\mathrm{mm}^2$, and the distance from the target center was 100 mm. This up and down configuration is the same as the decay counter (called CV) of KEK E548. The size and distance from the target center of

the left and right segments were $220 \times 400\,\mathrm{mm}^2$ and 200 mm, respectively. The thickness of these counters was 10 mm, and the signal was detected by fine-mesh-type PMTs (H6614-01MOD) on the downstream side.

3. Analysis

The missing mass, M_X, of the $^{12}\mathrm{C}(K^-,p)X$ reaction is reconstructed as

$$M_X = \{(E_K + M(^A Z) - E_p)^2 - (p_K^2 + p_p^2 - 2p_K p_p \cos\theta_{Kp})\}^{1/2}, \tag{3}$$

where E_K and p_K are the energy and momentum of the beam K^- in the laboratory frame, E_p and p_p are those of the outgoing proton, Z denotes the proton number of the target material, $M(^A Z)$ is the mass of the target, and θ_{Kp} is the scattering angle of the (K^-,p) reaction. Therefore, we must measure three kinematic variables, p_K, p_p, and θ_{Kp}, through the momentum reconstruction after the event selection. Once the missing mass is calculated, the K^--binding energy, B_K, can be obtained as

$$B_K = M(^{(A-1)}(Z-1)) + M_K - M_X. \tag{4}$$

Here, $M(^{(A-1)}(Z-1))$ and M_K are the masses of the core nucleus and K^-.

The double differential cross section $(d^2\bar{\sigma}/d\Omega/dM)_{\theta_1-\theta_2}$ for the $^{12}\mathrm{C}(K^-,p)X$ reaction averaged over the scattering angle from θ_1 to θ_2 can be evaluated, as a function of the missing mass, as

$$\left(\frac{d^2\bar{\sigma}}{d\Omega dM}\right)_{\theta_1-\theta_2} = \frac{A}{N_\mathrm{A}(\rho x)} \frac{N_{Kp}}{N_\mathrm{beam}\Delta\Omega_{\theta_1-\theta_2}\Delta M \epsilon}, \tag{5}$$

where A is the mass number of the target, N_A is Avogadro's number, ρx is the target thickness, N_{Kp} is the number of good (K^-,p) events in the missing-mass interval ΔM, N_beam is the number of beam kaons on the target, $\Delta\Omega_{\theta_1-\theta_2}$ is the effective solid angle of the SKS between θ_1 and θ_2, and ϵ is the total experimental efficiency.

The details of the analysis strategy of SKS at the J-PARC K1.8 beamline are also summarized in Refs. [31,32]. In this section, we describe the details of the analysis procedure.

3.1. Event selection and momentum reconstruction

Event selection and momentum reconstruction are performed step by step to calculate the missing mass, as described below. First, (K^-,p) events should be distinguished from background events. All counters must give signals, and the beam K^- and outgoing protons are selected. Next, momentum reconstruction for the beam and outgoing particles is performed. After the momentum reconstruction, we identify the outgoing protons by the time of flight along with the reconstructed flight path and momentum. Moreover, we reconstruct the vertex point and scattering angle of the (K^-,p) reaction to eliminate background events not originating from the target. Then, the final candidate events are chosen to calculate the missing mass.

The beam K^- was selected by requiring anti-coincidence of the BACs as BH2 $\times$ $(\overline{\mathrm{BAC1} \parallel \mathrm{BAC2}})$ at the trigger level. In the offline analysis, the K^- is identified by requiring no TDC hit of the BACs within a time window as narrow as 10 ns, regarding the beam timing measured by BH2, to reduce the number of K^- beam events vetoed by accidental pions. Moreover, the time of flight, tof_beam, between BH1 and BH2 with a flight path of 10.4 m is also used for K^- selection.

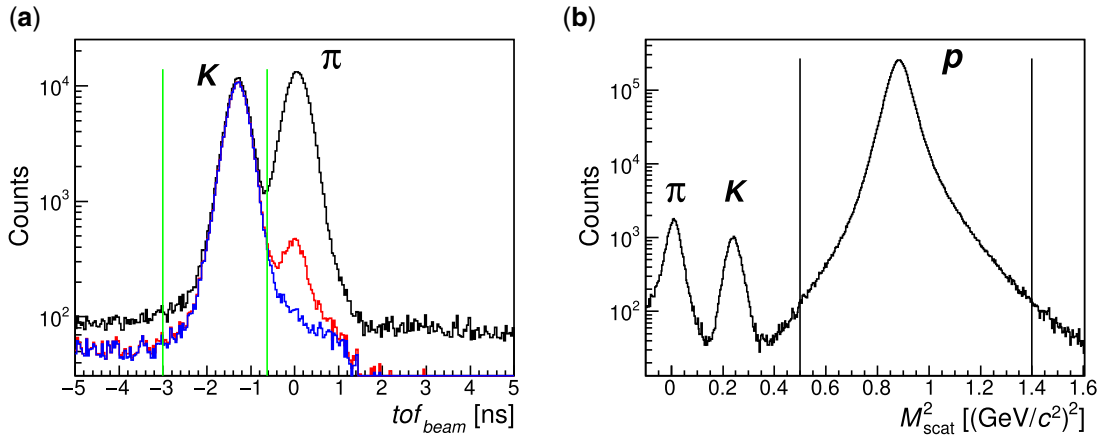

Fig. 4. (a) Typical time of flight, $tof_{\rm beam}$, spectra of the incident beam particles. The black spectrum shows the raw time of flight obtained by requiring only the hits of BH1 and BH2. The red and blue spectra show the time of flight with the BAC selection at the trigger and offline levels, respectively. (b) Typical squared mass, $M^2_{\rm scat}$, distribution of the outgoing particles.

Figure 4(a) shows the typical time-of-flight spectra. The black spectrum shows the raw time of flight obtained by requiring only hits of BH1 and BH2. The time offset is adjusted to $tof_{\rm beam} = 0$ for the pion beam. The red and blue spectra are obtained with the BAC selection at the trigger and offline levels, respectively. The time window for the K^- selection, $-3 < tof_{\rm beam} < -0.62$ ns, is also shown by the green lines. The lower limit is loosely set because there is no background contribution. On the other hand, a stricter upper limit, corresponding to $+3\,\sigma$, is set to avoid the background due to the remaining pions in the beam, even though most of the pion components are suppressed by the BAC selection. The pion contamination after the K^- beam selection is suppressed, as shown by the blue distribution.

The beam momentum is reconstructed using information from particle trajectories detected by BFT and the BCs. We call this procedure K1.8 tracking, whose details are described in Ref. [32]. The horizontal hit position upstream of the *QQDQQ* magnets was measured by the BFT. We select BFT hits with a time window of ± 4 ns relative to the beam timing measured by BH2. Moreover, the hit position matching the BH1 hit segment is also required to suppress accidental hits. The particle trajectories downstream of the magnets are reconstructed from a local track of the BCs, determined by linear least-squares fitting. We also require consistency between the reconstructed trajectory and the BH2 track segment. After selecting the track candidates, the beam momentum is evaluated using the third-order transfer matrix calculated using the ORBIT code (S. Morinobu, private communication). In this analysis, multi-track events are discarded after evaluating the consistency with the BH1 and BH2 hit segments.

The momentum of an outgoing particle is reconstructed with the hit information of SDC1–SDC4. The local straight tracks at the upstream (SDC1 and SDC2) and downstream (SDC3 and SDC4) drift chambers select the proper hit candidates for the momentum analysis. We also evaluate the consistency between the reconstructed trajectories of the downstream local track and TOF hits. After these selections, the hit position at each layer of SDC is connected using the Runge–Kutta method [33]. In this procedure, called SKS tracking, the momentum vector of the outgoing particle is reconstructed. Figure 5 shows a typical reduced χ^2 distribution of the SKS tracking. A reduced χ^2 value of less than 30 is accepted for the analysis.

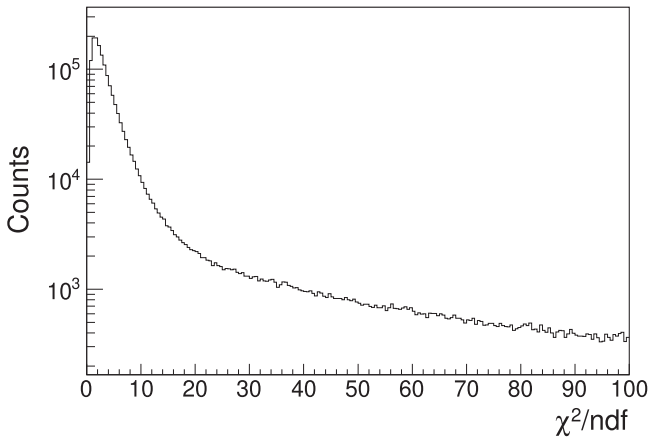

Fig. 5. A typical reduced χ^2 distribution of the SKS tracking.

The outgoing proton is identified by selecting a region of the squared mass spectrum, $M^2_{\rm scat}$, calculated as

$$M^2_{\rm scat} = \left(\frac{p}{\beta}\right)^2 (1-\beta^2), \tag{6}$$

where p is the reconstructed momentum as described above, and β is the velocity of the outgoing particle calculated using the flight path length and time of flight between BH2 and TOF. Figure 4(b) shows a typical squared mass spectrum. The outgoing proton is chosen with the selection gate $0.5 < M^2_{\rm scat} < 1.4\,({\rm GeV}/c^2)^2$, as shown by the black lines. The $M^2_{\rm scat}$ cut efficiency is estimated to be 99.8%. The background contamination in the selection gate is negligibly small because the π^+ produced from the target and in-flight decay of K^- was strongly suppressed by AC at the trigger level.

The reaction vertex point and the scattering angle of the (K^-, p) reaction are reconstructed from both the incident beam and outgoing particle trajectories obtained from the straight-line tracking of the BCs and SKS tracking, respectively. The vertex information suppresses background not originating from the target. Figure 6(a) shows the distribution of the z-coordinate (beam direction) of the vertex point. In this z-vertex spectrum, events with a scattering angle of $3.5^\circ < \theta_{Kp} < 4.5^\circ$ and binding energy of $B_K > -100$ MeV are selected.

We set a window of $-100 < z < 200$ mm for the z-vertex, as shown by the black lines. This window is set wider than the actual target lengths of 54.2 mm (^{12}C graphite) and 100.0 mm (CH_2), to keep a sufficient vertex-cut efficiency. Figure 6(b) shows the scattering angle dependence of the vertex-cut efficiency for the graphite target. The efficiency reaches a plateau ($\epsilon_{\rm vertex} \sim 99.6\%$) at $\theta_{Kp} \sim 8^\circ$. This efficiency curve corrects the cross section value event by event once the θ_{Kp} angle is calculated. The efficiencies are evaluated and applied separately for the CH_2 target data. The background contamination in this z-vertex window around $\theta_{Kp} \sim 4^\circ$ is negligible because the distance between the downstream edge of BAC ($z \sim -400$ mm) and the lower bound of the z-vertex gate ($z = -100$ mm) is approximately 300 mm, corresponding to more than $10\,\sigma$ with the z-vertex resolution of $\sigma \sim 28$ mm at $\theta_{Kp} \sim 4^\circ$.

We do not introduce the vertex cut of the x (horizontal) and y (vertical) coordinates because the target ($150^x \times 50^y$ mm^2) is sufficiently larger than the K^- beam profile, whose typical size is 21.7 mm

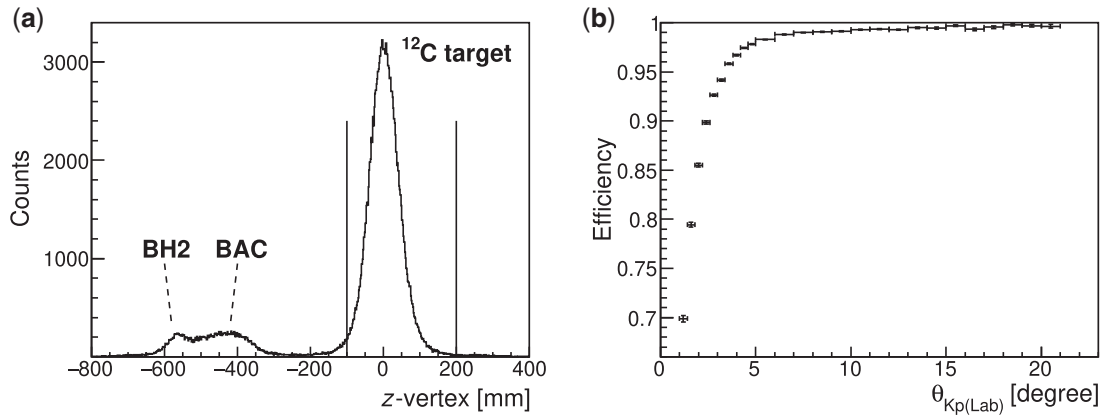

Fig. 6. (a) Distribution of the z-coordinate of the reaction vertex point, z-vertex, in the scattering angle interval $3.5^\circ < \theta_{Kp} < 4.5^\circ$ and for $B_K > -100$ MeV. The dashed line shows the detector positions around the target. The black lines show the window for the z-vertex selection. (b) The obtained vertex selection efficiency for the ^{12}C graphite target data as a function of the scattering angle.

(x) and 3.5 mm (y) in σ. Then, the final (K^-, p) events are selected to calculate the missing mass following Eq. (3).

3.2. Momentum correction

We apply three types of momentum correction. First, the momentum correction of the outgoing particle is performed to cure the correlation with the scattering angle and evaluate the missing-mass resolution. Next, the energy loss in materials such as the experimental target is corrected. Finally, we correct the momenta of both the beam and the outgoing particles to obtain accurate absolute momenta by using the beam pass-through and CH_2 target data.

In the present analysis, the outgoing particles are reconstructed by using the calculated field map for the SKS magnet. However, this calculated field map may not completely reproduce the real one, and this effect may cause some correlations. Therefore, we introduce phenomenological correction terms (we call it *uv* correction) as a momentum calibration as

$$p'_{\mathrm{SKS}} = p_{\mathrm{SKS}} + f(u) + g(v), \tag{7}$$

$$f(u) = A_5 u^5 + A_4 u^4 + A_3 u^3 + A_2 u^2 + A_1 u, \tag{8}$$

$$g(u) = B_4 v^4 + B_3 v^3 + B_2 v^2 + B_1 v, \tag{9}$$

where p'_{SKS} and p_{SKS} are momenta of the outgoing particle after and before the correction, respectively. Here, u and v are the horizontal (dx/dz) and vertical (dy/dz) direction cosines of the outgoing particle at the target position, respectively. The polynomial functions $f(u)$ and $g(v)$ remove the correlation. $A_{1\text{–}5}$ and $B_{1\text{–}4}$ are the parameters calculated by using the K^- elastic scattering peak in the missing mass spectrum of the $p(K^-, p)K^-$ reaction for the CH_2 target data. In the *uv* correction, we do not introduce zeroth-order terms, A_0 and B_0, in the polynomials corresponding to the absolute momentum scale because the absolute momentum is corrected with the final momentum calibration, as described below.

After this step, the energy loss corrections for the experimental target, BH2, and BAC are applied. Energy loss correction is performed for each track by using the obtained momenta and reaction vertex. Correction values are calculated based on the Bethe–Bloch formula multiplied by a factor of 0.956,

which is evaluated from the beam pass-through data with and without the target. The same scale factor is applied for the BAC energy loss correction. The momentum difference, dp, is obtained by comparing the measured momenta of the K1.8 tracking and the SKS tracking as $dp = p_{\rm SKS} - p_{K1.8}$. Moreover, since each BH2 segment had overlaps by 5 mm at the edge, we can easily observe double peak structures in the dp spectrum. From these peaks, we can also estimate the energy loss in the BH2.

The absolute momentum scales of the beam and outgoing particles are adjusted using the beam pass-through data and the K^- and Ξ^- peaks of the $p(K^-,p)K^-$ and $p(K^-,K^+)\Xi^-$ reactions, respectively, collected using the CH_2 target at $p_{K^-} = 1.8\,{\rm GeV}/c$. Regarding the absolute momentum correction, second- and third-order polynomial functions are introduced for the beam and outgoing particles, reducing dp of the beam pass-through data and the differences in the K^- and Ξ^- masses between the Particle Data Group value and the measured value. A similar momentum correction was applied in the J-PARC E10 analysis, and the detailed correction procedure was described in Ref. [32]. After the absolute momentum adjustment, the differences between the ideal and corrected momenta are reduced within $\pm 0.3\,{\rm MeV}/c$. The remaining differences are a systematic uncertainty on the momentum reconstruction. Finally, the systematic uncertainty in the binding energy of the $^{12}{\rm C}(K^-,p)$ reaction around the threshold, $B_K \sim 0$, is estimated as 0.3 MeV.

3.3. *Efficiency evaluation*

After we select the (K^-,p) events and correct the momenta, the double differential cross section defined in Eq. (5) is estimated; ϵ in Eq. (5) shows the overall experimental efficiency resulting from DAQ, detectors, and analysis cuts. It is the result of several terms, some of which depend on the experimental conditions and are applied event by event ($\epsilon_{\rm evt}$), while the others are common to all events and are applied in the final phase of the analysis ($\epsilon_{\rm com}$).

First, we describe the contributions to common efficiency ($\epsilon_{\rm com}$). The data acquisition efficiency, $\epsilon_{\rm DAQ}$, is evaluated as the probability of accepting the trigger determined by the dead time of the data acquisition system. Its value is estimated as $\epsilon_{\rm DAQ} = 66.4 \pm 0.8\%$, where the error comes from the stability of the data acquisition system. The beam K^- selection efficiency is defined as $\epsilon_{\rm beam} = N(K^-\ \text{selection})/N(K^-\ \text{beam trigger})$, where $N(K^-\ \text{beam trigger})$ is the number of K^- beam particles at the trigger level defined as BH2 $\times$ $(\overline{\rm BAC1 \parallel BAC2})$. $N(K^-\ \text{selection})$ shows the number of beam K^- selected during the offline analysis, as described in Sect. 3.1. Thus, $\epsilon_{\rm beam}$ includes the hit efficiency of BH1. The efficiency is evaluated as $\epsilon_{\rm beam} = 92.1 \pm 0.1\%$. The error is estimated from the fluctuations during the data recording period. Moreover, we discard events with double BH2 hits, although we lose a small fraction of good events where the beam particle passes through the two adjacent modules of BH2 overlapping by 5 mm. This way, we avoid the event-by-event double energy-loss correction for BH2. The ratio of double-to-single BH2 hit events in the ^{12}C target data is $7.94 \pm 0.13\%$, where the error is estimated by changing the other cut conditions, such as those with and without the (K^-,p) selection.

The local tracking efficiency for each set of chambers is evaluated to be $\epsilon_{\rm BFT} = 94.8 \pm 0.5\%$, $\epsilon_{\rm BC3\text{–}4} = 93.8 \pm 0.5\%$, $\epsilon_{\rm SDC1\text{–}2} = 96.3 \pm 0.6\%$, and $\epsilon_{\rm SDC3\text{–}4} = 99.4 \pm 0.1\%$. The efficiencies of BFT ($\epsilon_{\rm BFT}$) and BC3–BC4 ($\epsilon_{\rm BC3\text{–}4}$) are estimated using the events collected with the BH2 self-trigger that was mixed during the physics data collected to obtain the unbiased data from the K^- beam. We select the single-track candidates for the analysis of BFT and BC3 and 4 after requiring hit consistency with BH1 and BH2, respectively. The efficiency of SDC1–SDC2 ($\epsilon_{\rm SDC1\text{–}2}$) is obtained using the events collected with the BH2 self-trigger. Here, we select the events in which KIC had no hit to select the

Table 1. The efficiency of SKS tracking for each scattering angle.

θ_p [degree]	1–3	3–5	5–7	7–9	9–11
$\epsilon_{\text{SKS track}}$ [%]	91.5 ± 0.1	91.5 ± 0.0	91.2 ± 0.2	90.9 ± 0.3	$90.3\,^{+0.4}_{-0.5}$
θ_p [degree]	11–13	13–15	15–17	17–19	19–21
$\epsilon_{\text{SKStrack}}$ [%]	89.2 ± 0.4	$88.0\,^{+0.5}_{-0.6}$	$86.3\,^{+0.5}_{-0.7}$	$81.7\,^{+2.2}_{-3.6}$	$72.0\,^{+5.6}_{-12.1}$

beam pass-through events and discard the scattering events on the target material. The consistency of the efficiency evaluation is checked by using the events corrected with the (K^-, π^+) trigger defined as K$\pi \equiv$ BEAM $\times$ TOF $\times$ AC $\times$ LC $\times$ MT. The efficiency of SDC3–SDC4 is estimated by using the (K^-, p) events because the protons are free from decay in flight. In this efficiency evaluation, the outgoing proton is selected using the information from the horizontal direction cosine (dx/dz) of the SDC1–SDC2 local track and time of flight (BH2–TOF). The errors of these local track efficiencies are estimated from the fluctuation during the data-collection period.

Other common efficiencies are the TOF efficiency, proton identification efficiency of AC, proton selection efficiency, proton absorption, and K^- beam survival factor. The TOF efficiency is assumed to be $\epsilon_{\text{TOF}} = 100\%$. The proton identification efficiency of AC, which is decreased because of accidental veto by pions and δ-ray emission by protons, is evaluated to be $\epsilon_{\text{AC}} = 94.9 \pm 0.4\%$ using the events collected from the BH2 $\times$ TOF trigger. The proton selection efficiency with the selection gate of $0.5 < M^2_{\text{scat}} < 1.4\,(\text{GeV}/c^2)^2$, as shown in Fig. 4(b), is $\epsilon_{\text{PID}} = 99.8\%$. The proton absorption factor is estimated as $\epsilon_{\text{abs}} = 87.4 \pm 1.0\%$ by considering the total pN cross sections and material budget of the SKS system. The K^- beam survival factor, corresponding to the in-flight decay between BAC and the target, is evaluated as $\epsilon_{\text{surv}} = 96.8 \pm 1.0\%$. Then, the common efficiency is estimated as $\epsilon_{\text{com}} = 35.2 \pm 1.2\%$.

Next, we describe the efficiencies estimated for each event (ϵ_{evt}), namely those for SKS tracking (ϵ_{SKS}), LC (ϵ_{LC}), and vertex cut (ϵ_{vertex}). ϵ_{SKS} is the efficiency of the SKS tracking for the momentum evaluation of the outgoing particles using the Runge–Kutta method. It is estimated using the (K^-, p) events as in the case of $\epsilon_{\text{SDC3–4}}$, and depends on the scattering angle (Table 1).

The efficiency of the LC trigger counter (ϵ_{LC}) is estimated using the (K^-, p) events collected using the BH2 $\times$ TOF trigger. It shows a momentum dependence for the outgoing protons for the SKS accepted momenta $p_{\text{SKS}} > 1.0\,\text{GeV}/c$. The efficiency around the acceptance edge of $1.0\,\text{GeV}/c$ is $\sim$75%, and improves to $\sim$95% at $1.2\,\text{GeV}/c$. ϵ_{LC} reaches a plateau, $\epsilon_{\text{LC}} \sim 98\%$, at $1.6\,\text{GeV}/c$. The region of interest around the threshold energy ($B_K \sim 0\,\text{MeV}$) in the $^{12}\text{C}(K^-, p)$ missing mass spectrum corresponds to an outgoing proton momentum of $\sim 2.0\,\text{GeV}/c$, which is significantly higher than the plateau region ($> 1.6\,\text{GeV}/c$). We apply the LC efficiency correction for each event according to the momenta of the outgoing particles. Furthermore, the vertex-cut efficiency correction is applied for each event according to the scattering angles (Sect. 3.1 and Fig. 6).

The effective solid angle of the SKS system, $\Delta\Omega_{\theta_1-\theta_2}$, is evaluated using a Monte Carlo simulation. The solid angle as a function of the momentum and scattering angle of the outgoing particles is defined as

$$\Delta\Omega_{\theta_1-\theta_2}(p) = 2\pi \int_{\theta_1}^{\theta_2} d\cos\theta \times \epsilon_{\text{Acc}}(p, \theta), \tag{10}$$

$$\epsilon_{\text{Acc}}(p, \theta) = \frac{N(\text{accepted events})}{N(\text{generated events})}. \tag{11}$$

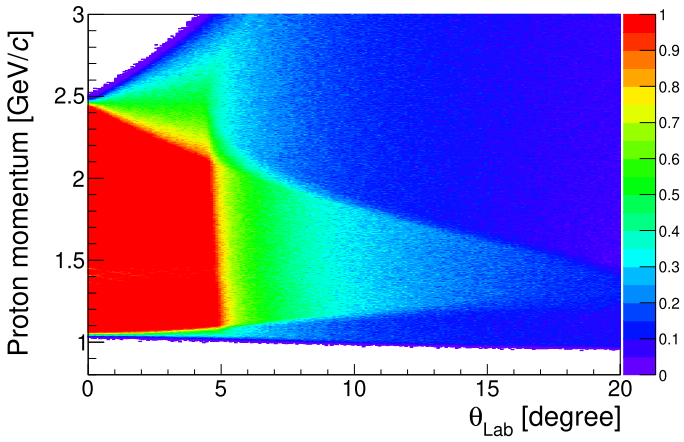

Fig. 7. SKS acceptance as functions of the momentum and scattering angle of the outgoing particle.

We set a fixed interval of $\Delta\theta$ as $\theta_1 - \theta_2 = \Delta\theta$. N(accepted events) and N(generated events) are the number of protons accepted and generated in the Monte Carlo simulation, respectively. Figure 7 shows the obtained acceptance as a function of the momentum and the scattering angle of the outgoing particles. The SKS has a large momentum acceptance in the range 1.1–2.5 GeV/c. The momenta of the outgoing protons at 0° are 2.05 GeV/c for the $p(K^-,p)K^-$ elastic scattering, 2.11 GeV/c for the $^{12}\mathrm{C}(K^-,p)^{11}\mathrm{B} + K^-$ threshold ($B_K = 0$ MeV), and 2.32 GeV/c for the deeply bound ($B_K \sim 200$ MeV) region of the kaonic nucleus. Thus, the SKS has sufficient acceptance to study the $\bar{K}$–nucleus potential when we select forward-scattering angles.

4. Experimental results

First, we show the proton target data at $p_{K^-} = 1.8$ GeV/c. Figure 8 shows the double differential cross section as a function of the missing mass $M_{(K^-,p)}$ for the CH_2 and ^{12}C targets plotted with green and red points, respectively. The missing mass ($M_{(K^-,p)}$) is calculated in the kinematics for a proton at rest as the target, as $M_{(K^-,p)} = \{(E_K + M_p - E_p)^2 - (p_K^2 + p_p^2 - 2p_K p_p \cos\theta_{Kp})\}^{1/2}$. The black distribution corresponds to the hydrogen target spectrum and was obtained by subtracting the ^{12}C contribution from the CH_2 target spectrum. In the subtraction, we set the target mass number (A) in Eq. (5) equal to 14 for the CH_2 and 12 for the ^{12}C targets in this analysis. The reported errors are statistical. The systematic uncertainty for the absolute cross section due to the uncertainty in the efficiency, described in Sect. 3.3, is evaluated as 3.5%.

In these spectra, we choose the forward-scattering angle range $3.5° < \theta_{Kp(\mathrm{Lab})} < 4.5°$, as in the $^{12}\mathrm{C}(K^-,p)$ analysis. This scattering angle is selected to use low momentum-transfer events.[2] We discard the very forward region where the background contamination dominates because of the worsened z-vertex resolution. Moreover, the selection $3.5° < \theta_{Kp(\mathrm{Lab})} < 4.5°$ is suitable to directly compare the obtained spectrum and the theoretical one at $\theta_{Kp(\mathrm{Lab})} = 4°$. We ensure that the spectrum shape does not change when we choose a tighter angle cut $3.9° < \theta_{Kp(\mathrm{Lab})} < 4.1°$.

Figure 9 shows the $p(K^-,p)$ reaction cross section as a function of the missing mass ($M_{(K^-,p)}$). The black points with error bars show the experimental values. This spectrum was obtained from the hydrogen target contribution (the black points in Fig. 8) by scaling it by a factor of two to consider the difference in the number of proton targets. The contribution of each reaction process is obtained

[2] In the case of KEK E548, the scattering angle range $0° < \theta_{Kp(\mathrm{Lab})} < 4.1°$ was chosen.

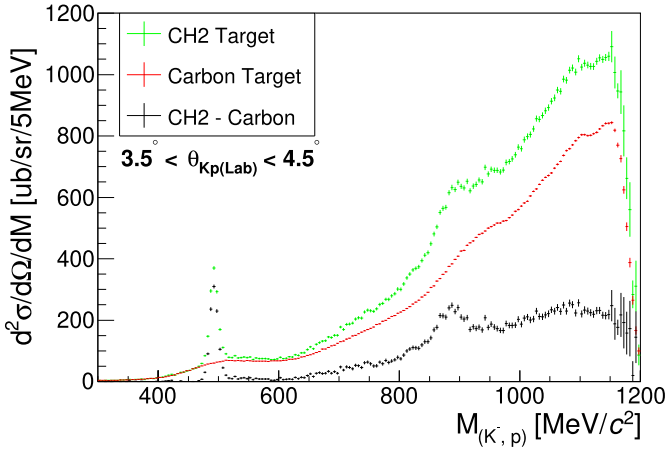

Fig. 8. Double differential cross section as a function of the missing mass, $M_{(K^-,p)}$. The green and red spectra show the CH_2 and ^{12}C target data, respectively. In this analysis, we adopt the target mass number (A) in Eq. (5) as 14 for the CH_2 and 12 for the ^{12}C targets. The hydrogen target data, shown by the black spectrum, are obtained by subtracting the ^{12}C spectrum from the CH_2 target spectrum.

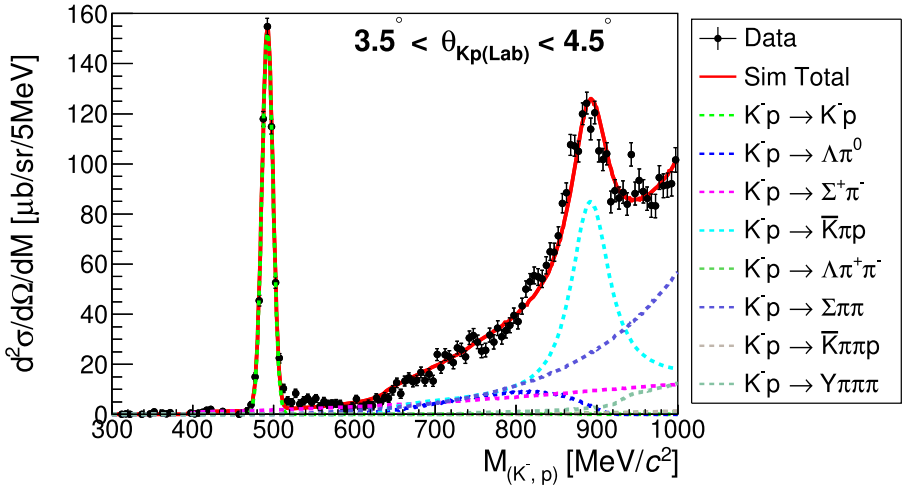

Fig. 9. The $p(K^-,p)$ cross section as a function of $M_{(K^-,p)}$ at 1.8 GeV/c is shown by black points with statistical errors. This spectrum is obtained from the hydrogen target data (the black points in Fig. 8) by scaling it by a factor of two to consider the difference in the number of proton targets. The spectrum is fitted with the template distributions, as shown by the dashed lines with different colors in the figure. The red line displays the total fit result.

by fitting the data with the calculated spectral shape (called "templates" hereafter) of all processes, where the following reaction processes are considered: $K^-p \to pK^-$ (elastic), $\Lambda\pi^0$, $\Sigma^+\pi^-$, $\bar{K}\pi p$, $\Lambda\pi^+\pi^-$, $\Sigma\pi\pi$, $\bar{K}\pi\pi p$, $\Lambda\pi\pi\pi$, and $\Sigma\pi\pi\pi$. In this fit, the cross section of each reaction process is considered as a free parameter. The template distributions are derived from a Monte Carlo simulation. The fit results are shown in the figure by dashed lines of different colors.

In these templates, outgoing protons originating from hyperon decays such as $K^-p \to \Lambda\pi^0, \Lambda \to p\pi^-$ are also considered. Moreover, resonance production processes, such as $K^-p \to K^*(890)^-p \to \bar{K}\pi p$, $K^-p \to Y^*\pi \to (\bar{K}\pi p)$ or $(Y\pi\pi(\pi))$, and $K^-p \to \bar{K}\Delta(1232) \to \bar{K}\pi p$, are also included. Here, Y^* (Y) stands for excited states of hyperons such as $\Lambda(1520)$ and $\Sigma(1385)$ (ground state hyperon, Λ or Σ). We combine the non-resonant and resonant production processes for the same final

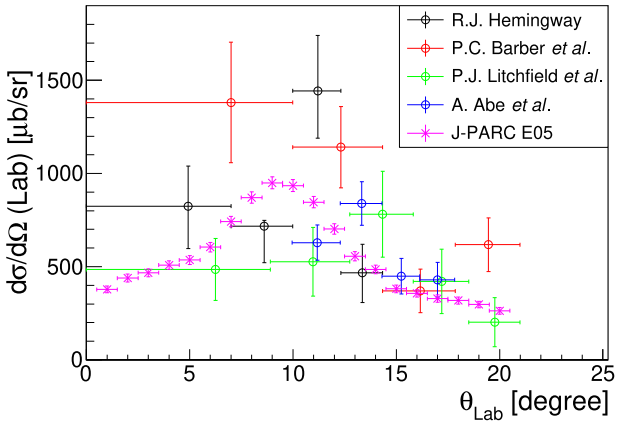

Fig. 10. Compilation of differential cross sections of the K^-p elastic scattering at $p_{K^-} = 1.8\,\mathrm{GeV}/c$. Our results are shown by the magenta points with statistical errors. The previous data [44–47] are also displayed in different colors.

states based on the differential cross section for each process measured by the previous experiments [34–43]. This helps to reduce the number of fit parameters. Finally, we find a reasonable fit to the $p(K^-,p)$ spectrum, as shown by the red line.

We observe a clear peak around $M_{(K^-,p)} \sim 494\,\mathrm{MeV}/c^2$ in Fig. 9, corresponding to the K^- mass coming from the $p(K^-,p)K^-$ elastic process. The green dashed line in Fig. 9 shows the elastic component. This peak has a width of $7.1\,\mathrm{MeV}/c^2$ (σ), from which the missing mass resolution of the $^{12}\mathrm{C}(K^-,p)$ reaction is estimated to be 4.2 MeV (σ) around the threshold ($B_K \sim 0\,\mathrm{MeV}$). The differential cross section of the elastic scattering is derived by integrating the green dotted line and obtained values for various scattering angles, and is shown by the magenta points with statistical error bars in Fig. 10. In this figure, the differential cross sections measured by previous experiments [44–47] are also shown in other colors. The evaluated differential cross section is also listed in Appendix A. We observe reasonable agreement with the past results, even though the statistical precision of the previous data is not so high.

Next, we show the $^{12}\mathrm{C}(K^-,p)$ spectrum at $p_{K^-} = 1.8\,\mathrm{GeV}/c$ as a function of the K^--binding energy, B_K (Fig. 11). The black points with statistical error bars show the measured spectrum. The systematic uncertainty of the binding energy around the threshold ($B_K \sim 0\,\mathrm{MeV}$) is estimated to be 0.3 MeV (Sect. 3.2). We selected the forward-scattering angle range $3.5° < \theta_{Kp(\mathrm{Lab})} < 4.5°$ in this analysis. We compare the spectrum with the template for the quasi-free elastic K^-p scattering without secondary interactions inside the target nucleus. Here, the secondary interaction means the interaction between the recoiling K^- at the first step K^-"p" $\to K^-p$ reaction and the residual ^{11}B nucleus. The template for the quasi-free elastic K^-p scattering without secondary interactions is derived by using the Green's function method with the set of parameters V_0 (real part) = W_0 (imaginary part) = 0 MeV. Details of the calculation method are described in Sect. 5.1.

The green dotted line (K^-"p" (QF-Elastic)) in Fig. 11 displays the quasi-elastic component. We also consider inelastic processes in quasi-free K^-+"p" reactions that can be estimated from our $K^- + p$ data shown in Fig. 9.[3] The mixed inelastic K^-+"p" component is displayed by a blue dotted

[3] The cross sections of the inelastic processes are fixed by normalizing to the elastic process. For example, the contributions of K^-"p" $\to \Lambda\pi^0$, $\Lambda \to p\pi^-$ and K^-"p" $\to \bar{K}\pi p$, are fixed by our proton target data. The resonance, such as Y^* and K^*, production processes are also included as in the proton target analysis.

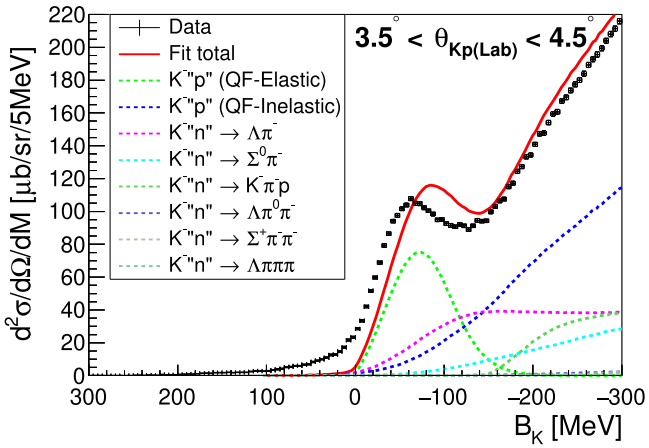

Fig. 11. Double differential ^{12}C(K^-,p) cross section as a function of K^- binding energy, B_K. The forward scattering angle range of $3.5^\circ < \theta_{Kp(\mathrm{Lab})} < 4.5^\circ$ is selected. The black points with statistical error bars show the measured double differential cross section, and different colors show the template-fit results. The green dotted line shows the K^-"p" $\to K^-p$ quasi-elastic component, calculated by the Green's function method. In this fit, we do not include secondary interactions inside the target nucleus. See the details in the text.

line (K^-"p" (QF-Inelastic)). Furthermore, we must consider the quasi-free K^-+"n" reactions, such as K^-"n" $\to \Lambda\pi^-, \Lambda \to p\pi^-$, and K^-"n" $\to K^-\pi^-p$, whose cross sections are considered free parameters. In Fig. 11, the dotted lines with different colors show the quasi-free K^-+"n" contributions and a red line displays the total fit result. The templates of the quasi-free reactions are smeared out by considering the missing-mass resolution of 4.2 MeV (σ).

We find that the template can reasonably reproduce the highly unbound region ($B_K < -150$ MeV), where the inelastic processes (background) dominate. However, there exists a disagreement in the region of $B_K > -150$ MeV, where the quasi-elastic process is the main component. The χ^2/ndf of this fit in the region of $-300 < B_K < 40$ MeV is 300.9, where the number of degrees of freedom is $ndf = 61$. Note that we do not introduce any secondary interactions between the recoiling K^- and the residual ^{11}B nucleus in this fit. The effect of secondary interaction manifests itself in the ^{12}C(K^-,p) spectrum.

5. Theoretical investigation

It is essential to introduce the secondary interaction between the recoiling $\bar{K}$ and residual nucleus to reproduce the measured ^{12}C(K^-,p) spectrum. We calculate the ^{12}C(K^-,p) spectrum using the Green's function method [48] with various values of the $\bar{K}$–nucleus potential. We follow the procedure of our previous theoretical framework [48] with a little modification to add a kinematical correction factor K. We can search for the optimum parameters by comparing the measured and calculated spectra.

5.1. Theoretical calculation

We theoretically evaluate the double differential cross section of the (K^-,p) reaction on a nuclear target using the Green's function method. In this method, we factorize the reaction cross section into the nuclear response function $S(E)$ and elementary cross section of the $p(K^-,p)K^-$ reaction with

the impulse approximation,

$$\left(\frac{d^2\sigma}{d\Omega dE}\right)_A^{\rm lab} = \left(\frac{d\sigma}{d\Omega}\right)_{\rm ele}^{\rm lab} \times S(E). \tag{12}$$

In this framework, the elementary cross section determines the absolute size of the reaction cross section. In this analysis, the absolute size is one of the fitting parameters to reproduce the data at a satisfactory level. The nuclear response function $S(E)$ is written as

$$S(E) = -\frac{1}{\pi}{\rm Im}\sum_f K \int d\boldsymbol{r}d\boldsymbol{r}'\tau_f^\dagger(\boldsymbol{r})G(E;\boldsymbol{r},\boldsymbol{r}')\tau_f(\boldsymbol{r}'), \tag{13}$$

where the summation is taken over all possible final states. K is the kinematical correction factor, which is included to modify our theoretical framework in Ref. [48] and is defined as

$$K = \left[\frac{|\boldsymbol{p}'_p{}^A|}{|\boldsymbol{p}'_p|}\frac{E_pE'_K}{E_p^AE_K'^A}\left(1+\frac{E'_p}{E'_K}\frac{|\boldsymbol{p}'_K|-|\boldsymbol{p}_p|\cos\theta_{Kp}}{|\boldsymbol{p}'_p|}\right)\right]^{\rm lab}, \tag{14}$$

where the superscript A shows that the momenta and energies are evaluated in the kinematics of the nuclear target [49]. E and E' are the energies of incident and emitted particles, respectively. The same holds for the momenta $\boldsymbol{p}$ and $\boldsymbol{p}'$. The superscript "lab" shows that the kinematical variables are evaluated in the laboratory frame.

The amplitude τ_f denotes the transition of the incident particle (K^-) to the proton hole and outgoing particle (p), involving the proton-hole wave function ψ_{j_p} and distorted waves, χ_i and χ_f, of the projectile and ejectile taking the appropriate spin sum

$$\tau_f(\boldsymbol{r}) = \chi_f^*(\boldsymbol{r})\xi^*_{1/2,m_s}[Y^*_{l_K}(\hat{\boldsymbol{r}})\otimes\psi_{j_p}(\boldsymbol{r})]_{JM}\chi_i(\boldsymbol{r}) \tag{15}$$

with the meson angular wave function $Y_{l_K}(\hat{\boldsymbol{r}})$ and spin wave function $\xi^*_{1/2,m_s}$ of the ejectile. The momentum distributions of the nucleons inside the target nucleus are determined by their harmonic oscillator wave functions in the coordinate space. The distorted waves are written with the distortion factor $F(\boldsymbol{r})$ as

$$\chi_f^*(\boldsymbol{r})\chi_i(\boldsymbol{r}) = \exp(i\boldsymbol{q}\cdot\boldsymbol{r})F(\boldsymbol{r}), \tag{16}$$

with the momentum transfer $\boldsymbol{q}$. The distortion factor $F(\boldsymbol{r})$ is defined as

$$F(\boldsymbol{r}) = \exp\left[-\frac{1}{2}\bar{\sigma}\int_{-\infty}^{\infty}dz'\bar{\rho}(z',\boldsymbol{b})\right], \tag{17}$$

where $\bar{\sigma}$ is the averaged distortion cross section defined as

$$\bar{\sigma} = \frac{\sigma_{\bar{K}N}+\sigma_{pN}}{2}, \tag{18}$$

with the total cross sections of the incident kaon and emitted proton with the nucleons in the nucleus. The averaged nuclear density $\bar{\rho}(z',\boldsymbol{b})$ in Eq. (17) is given in the beam direction coordinate z', with impact parameter $\boldsymbol{b}$, by a modified harmonic oscillator distribution as

$$\bar{\rho}(r) = \rho_0\left[1+\bar{a}\left(\frac{r}{\bar{R}}\right)^2\right]\exp\left[-\left(\frac{r}{\bar{R}}\right)^2\right] \tag{19}$$

in polar coordinates, with the averaged parameters $\bar{R}$ and $\bar{a}$ defined as

$$\bar{R} = \frac{R_i + R_f}{2} \tag{20}$$

and

$$\bar{a} = \frac{a_i + a_f}{2} \tag{21}$$

with the density parameters of the nuclei in the initial and final states. We use $R_i = 1.672$ fm, $R_f = 1.690$ fm, $a_i = 1.150$, and $a_f = 0.811$ [50].

The Green's function $G(E)$ contains the kaon–nucleus optical potential in the Hamiltonian H_K,

$$G(E, \boldsymbol{r}, \boldsymbol{r}') = \left\langle p^{-1} \left| \phi_K(\boldsymbol{r}) \frac{1}{E - H_K + i\epsilon} \phi^\dagger(\boldsymbol{r}) \right| p^{-1} \right\rangle, \tag{22}$$

where $\phi_K^\dagger$ is the kaon creation operator, and $|p^{-1}\rangle$ the proton-hole state [48,51,52]. The kaon energy E is defined as $E = T_K - T_p - S_p$, where T_K is the incident kaon kinetic energy, T_p the emitted proton kinetic energy, and S_p the proton separation energy from each proton single-particle level (see Table III of Ref. [53]).

Obtaining the Green's function with optical potential is essentially equivalent to solving the associated equation of motion, as explained in detail in Refs. [48,51,52,54]. We can calculate the nuclear response function $S(E)$ from $\tau_f^\dagger(\boldsymbol{r}) G(E; \boldsymbol{r}, \boldsymbol{r}') \tau_f(\boldsymbol{r}')$ by performing appropriate numerical integration for the variables $\boldsymbol{r}$ and $\boldsymbol{r}'$. In the Green's function formalism, we can calculate the response function $S(E)$ for both bound and quasi-free kaon production energy regions, and we perform the summation of the kaon final states without assuming the existence of discrete kaon-bound states, which could disappear in the case of the strongly absorptive optical potential.

As for the kaon–nucleus interaction, we parametrize the optical potential as

$$U(r, E) = (V_0 + iW_0 f_{\text{phase}}(E)) \frac{\rho(r)}{\rho(0)}, \tag{23}$$

and we introduce V_0 and W_0, showing the strength of the optical potential at the nuclear center, to analyze the experimental data and obtain new information on kaon–nucleus interaction. We use the same functional form as in Eq. (19) for the density distribution $\rho(r)$ in Eq. (23), and keep the same distributions for protons and neutrons. The point nucleon density distributions are deduced from $\rho(r)$ in Eq. (19) by using the prescription described in Ref. [55] to evaluate the kaon–nucleus optical potential. Notably, the imaginary part of the optical potential has an energy dependence via $f_{\text{phase}}(E)$ in this calculation [21,48]. Since the imaginary part of the potential describes the absorption of mesons followed by decay processes, such as $\bar{K} + N \to \pi + Y$ and $\bar{K} + N + N \to Y + N$, its energy dependence can be evaluated as a first approximation by the phase space volume of the decay processes. We consider two types of decay processes, mesonic decay $\bar{K} + N \to \pi + Y$ and non-mesonic decay $\bar{K} + N + N \to Y + N$, and introduce the energy dependence in the imaginary part by assuming the same dependence as the phase space volume of each process. We also assume that the branching ratios of mesonic (1N absorption) and non-mesonic (2N absorption) decays are 80% and 20%, respectively, by referring to the data of the stopped K^- reaction [25].

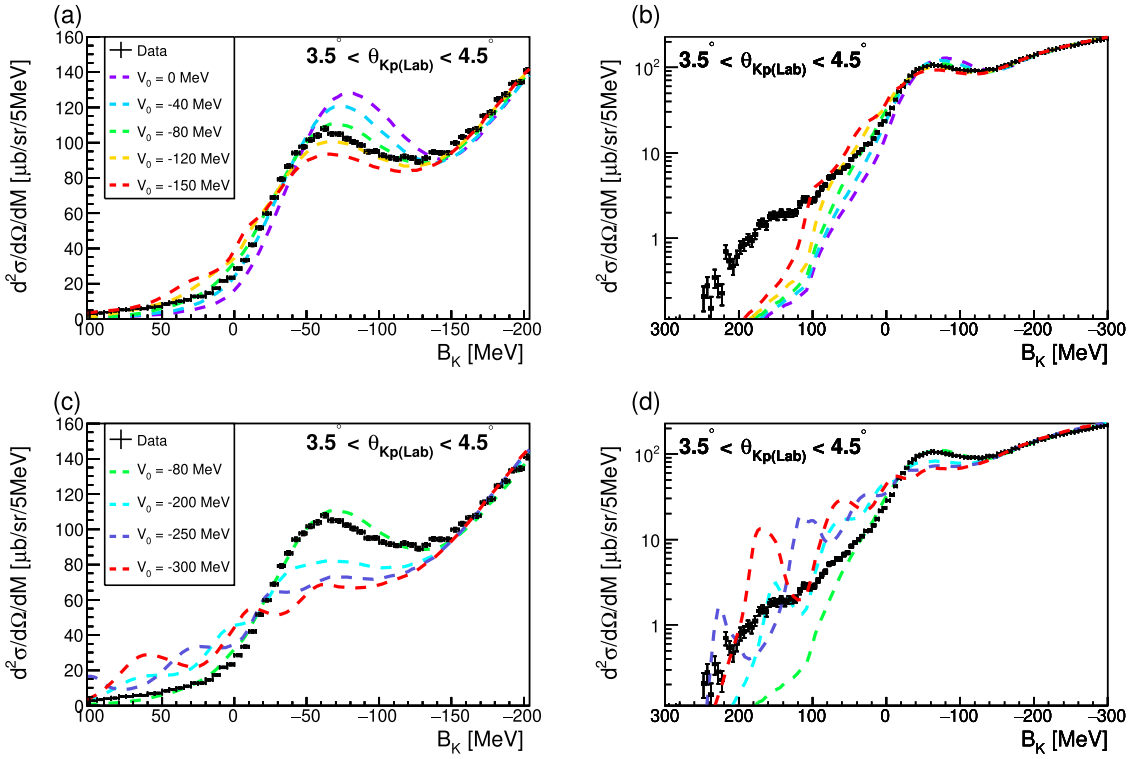

Fig. 12. Comparison between the measured spectrum and template fit with different optical potentials. The black points with error bars display the measured spectrum. The dashed lines in different colors show the fit results using different potential depths of the real part (V_0). The imaginary part is fixed at the optimum value of $W_0 = -40$ MeV. The comparisons with the real part potentials of $V_0 = (0, -40, -80, -120, -150)$ MeV and $V_0 = (-80, -200, -250, -300)$ MeV are shown in (a, b) and (c, d), respectively. The spectra with linear and semi-log scale are shown in (a, c) and (b, d), respectively.

5.2. Comparison with the theoretical spectra

We compare the measured and theoretical spectra to search for the optimum parameters of the optical potential between $\bar{K}$ and the residual nucleus. Figure 12 shows a comparison between the present data and templates obtained by changing the optical potential parameters. Black points with error bars display the measured spectrum. In Fig. 12(a) and (b), each colored line corresponds to a different value of the real part of the optical potential, $V_0 = 0$, -40, -80, -120, and -150 MeV. The imaginary part is fixed at the optimum value of $W_0 = -40$ MeV.

The peak position of the quasi-elastic component, $B_K \sim -50$ MeV, and the yield ratio between the unbound ($B_K < 0$) and bound ($B_K > 0$) regions, strongly depend on V_0. Figure 12(a) shows that the measured spectrum is best reproduced with the potential depth $V_0 = -80$ MeV, where the χ^2/ndf of this fit in the region of $-300 < B_K < 40$ MeV is 17.2. The χ^2/ndf is 300.9 when we choose the parameter sets of $(V_0, W_0) = (0, 0)$ MeV as described in Sect. 4. The χ^2/ndf value is improved by introducing the secondary interaction between recoiling K^- and residual nucleus. Appendix B shows a detailed comparison between the measured spectrum and template fit with various $\bar{K}$–nucleus potentials. Since the optimum potential ($V_0 = -80$ MeV) is attractive, there exists a bound state in the calculated spectrum. The binding energy and decay width with the optimum potential parameters, $(V_0, W_0) = (-80, -40)$ MeV, are $B_K = 31$ MeV and $\Gamma = 53$ MeV, respectively. Appendix C describes the details of the calculated spectrum with the optimum potential parameters.

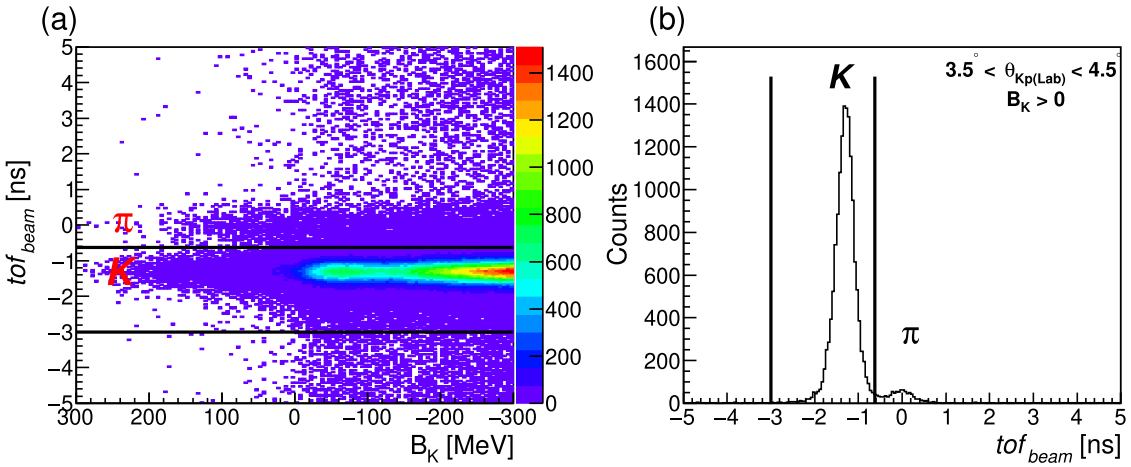

Fig. 13. (a) Two-dimensional plot between B_K and $tof_{\rm beam}$ of the incident beam particles. The time offset is adjusted to be $tof_{\rm beam} = 0$ for the pion beam. (b) The $tof_{\rm beam}$ spectrum when we choose the bound region, $B_K > 0$ MeV.

However, when we evaluate the deeply bound region $B_K \sim 100$ MeV, we find a significant enhancement in the measured spectrum from the fit result, as seen in Fig. 12(b) and the middle and right figures in Figs. B.1 and B.2. We need to adopt a much deeper real potential so as to reproduce the strength around the deeply bound region with this framework. Figure 12(c) and (d) show the template-fit results with very deep real potentials, $V_0 = -200$, -250, and -300 MeV. When we adopt such deep potentials, the yield around the deeply bound region becomes larger than the measured spectrum. However, such deep potentials can hardly reproduce the shallow bound region $B_K \sim 0$ MeV and quasi-elastic region $B_K \sim -50$ MeV. Consequently, it is challenging to reproduce the deeply bound, shallow bound, and unbound regions simultaneously with this framework. In the calculation with very deep real potential, structures resulting from the quasi-bound states of the kaonic nucleus appear because of the energy dependence of the imaginary potential via $f_{\rm phase}(E)$ in Eq. (23).

We evaluated the background of particle misidentification of the (K^-, p) reaction in order to confirm the enhancement in the deeply bound region. Figure 13(a) shows the two-dimensional plot between the K^- binding energy, B_K, and the time of flight, $tof_{\rm beam}$, of the incident beam particle. Figure 13(b) shows the $tof_{\rm beam}$ spectrum when we choose the bound region, $B_K > 0$ MeV. The black lines also display the time window for the K^- beam selection, $-3 < tof_{\rm beam} < -0.62$ ns. The background π^- beam contamination inside this time window is estimated to be 0.1% by selecting the bound region $B_K > 0$ MeV. Since the K1.8 beamline had two electrostatic separators (ESS1 and ESS2) and the pion detection efficiency of the BAC detector was high, the background π^- beam contamination is well suppressed. The background contamination for the outgoing proton selection is also negligibly small because the momentum of outgoing protons in the region of interest is $\gtrsim 2$ GeV/c and the momentum of outgoing K^+ and π^+ should be smaller than 1.7 GeV/c kinematically.

Moreover, we consider additional background because of the in-flight decay of beam K^-. The possible background reaction is $K^- \to \pi^-\pi^0$, π"p"$\to \pi p$. When the beam K^- decays between BAC and the experimental target, it could be misidentified as the beam K^-. However, the momentum of the scattered proton from this background reaction should be $\lesssim 2$ GeV/c because the momentum of π from the K^- decay is $\lesssim 1.7$ GeV/c. Therefore, this background does not affect the bound region $B_K > 0$ MeV.

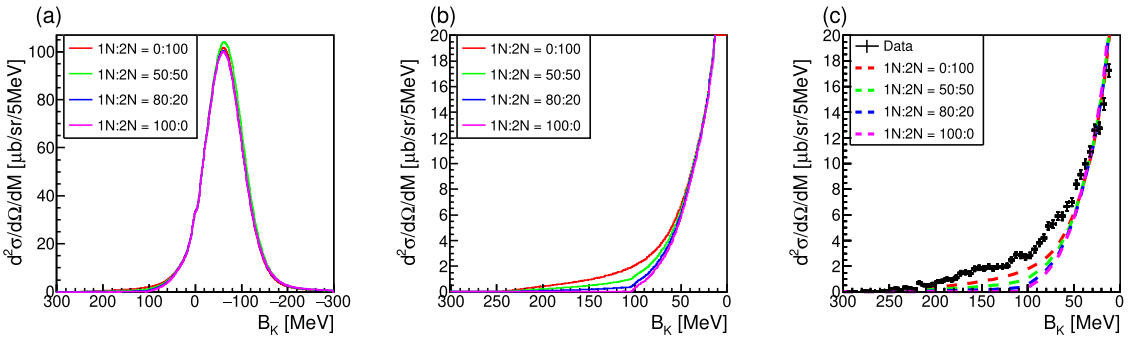

Fig. 14. (a) Calculated spectra by the Green's function method. The different colored lines correspond to the different values of the ratio between the 1N and 2N absorption. The parameters of the potential depth are fixed to the optimum values of $(V_0, W_0) = (-80, -40)$ MeV. (b) Magnified view of (a) to see the small cross section region. (c) Comparison between the measured spectrum and template fit result with different branching ratio values. The black points with error bars display the measured spectrum. The dashed lines in different colors show the fit results using different branching ratio values. Also in this fit, we fix the parameter of the potential depth as $(V_0, W_0) = (-80, -40)$ MeV.

Note that J-PARC E15 observed a significant event excess in the bound region as a long tail in the semi-inclusive ^{3}He(K^-, n) spectrum [56]. The background level in that region was rather high because of the background process K^-"N" $\to \pi\Sigma^+$, $\Sigma^+ \to \pi^+ n$, which has a long tail up to $B_K > 100$ MeV. Based on the kinematics of the different beam momenta, this background process does not contribute to our spectrum in the region $B_K > 100$ MeV. Note that we also consider these background processes of hyperon decays such as K^-"N" $\to \pi Y$, $Y \to \pi p$ in the template-fit analysis described above. Finally, we confirm that the contamination of the background in the deeply bound region is negligibly small and the enhancement originates from the ^{12}C(K^-, p) reaction.

6. Discussion

6.1. Interpretation by changing the branching ratio of 1N and 2N absorptions

We change the branching ratio of the mesonic (1N absorption) and non-mesonic (2N absorption) decays to reproduce the event excess in the deeply bound region. As described in Sect. 5.1, this branching ratio affects the imaginary part of the $\bar{K}$–nucleus potential. In the analysis performed so far, we assumed the branching ratio as 80% (1N absorption) and 20% (2N absorption) based on the previous data of the stopped K^- reaction [25]. Figure 14(a) shows the spectra calculated by changing the ratio between the 1N and 2N absorption processes. The parameters of the potential depth are fixed to the optimum values of $(V_0, W_0) = (-80, -40)$ MeV. Figure 14(b) shows a magnified view for the $B_K > 0$ MeV region. We find that the branching ratio does not significantly change the spectrum in the $B_K < 50$ MeV region. However, the spectrum in the deeply bound region is affected as shown (Fig. 14(b)). The yield around the deeply bound region becomes larger when we assume a larger branching ratio of the 2N absorption. Then, we perform a template fit by changing the branching ratio while fixing the parameters of the potential depth as $(V_0, W_0) = (-80, -40)$ MeV (Fig. 14(c)). The event around the deeply bound region can be partly explained when the branching ratio of the 2N absorption is large. However, even if we assume the extreme absorption ratio of (1N : 2N) = (0% : 100%), we cannot reproduce the deeply bound region well, as shown by the red dashed line.

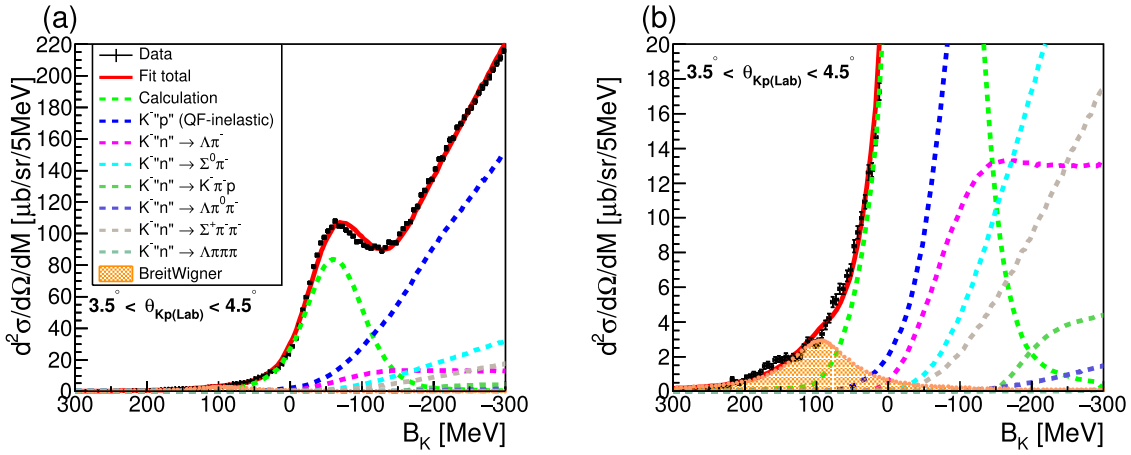

Fig. 15. (a) Template fit result by adding a Breit–Wigner function. The orange hatched spectrum displays the Breit–Wigner component. The green dashed line shows the calculated spectrum with the optical potential of $(V_0, W_0) = (-80, -40)$ MeV. The other color assignments are the same as in Fig. 11. (b) Magnified view of (a) for the small cross section region.

Moreover, we examine other background processes of one-step two-nucleon absorption and two-step three-nucleon absorption. Appendix D describes the details. Similar discussions are also given in Ref. [57]. We found that these background processes can also not explain the enhancement in the deeply bound region.

6.2. *Interpretation by introducing an additional resonant state*

Since it is not possible to reproduce the event excess in the present framework, we discuss its possible interpretation. We simply add a Breit–Wigner function in the fitting so as to reproduce the measured spectrum. Figure 15 shows the fitting result, where the orange hatched spectrum displays the Breit–Wigner component. The green dotted line shows the theoretical calculation with the optimum parameter set. The obtained χ^2/ndf values with and without the Breit–Winger function are 9.4 and 31.7, respectively.

Figure 16 shows the two-dimensional χ^2 plots as functions of the V_0 and W_0 parameters. Figure 16(a) shows the result without a Breit–Wigner function in the fitting region of $40 > B_K > -300$ MeV. In this fit, the enhanced deeply bound region is excluded. Figure 16(b) shows the result including a Breit–Wigner function. The white asterisk shows that the χ^2 minimum is found at $(V_0, W_0) = (-80, -40)$ MeV. The χ^2 distributions are essentially the same. By considering the χ^2 distribution, the statistical uncertainties of V_0 and W_0 are estimated to be ± 2 MeV. Moreover, the systematic uncertainties, which are evaluated by changing the fitting range and comparing the results with and without a Breit–Wigner function, as in Fig. 16(a) and (b), are ± 5 MeV for V_0 and ± 10 MeV for W_0. The optimum real potential, $V_0 = -80$ MeV, corresponds to the "shallow" potential predicted by the chiral models as described in Sect. 1. On the other hand, the "deep" potential, $V_0 \lesssim -150$ MeV, cannot reproduce the measured spectrum.

The peak position and width of the Breit–Wigner function are $B_K = 90$ MeV and $\Gamma = 100$ MeV, respectively. The statistical uncertainties on the peak position and decay width are less than ± 10 MeV. The production cross section of the Breit–Wigner component is obtained as $d\sigma/d\Omega \sim 80\,\mu\text{b}\,\text{sr}^{-1}$, where the statistical uncertainty is $\pm 3\,\mu$b/sr. The systematic uncertainties calculated by changing the fitting range are also less than ± 10 MeV. By changing the branching ratio between the 1N and 2N

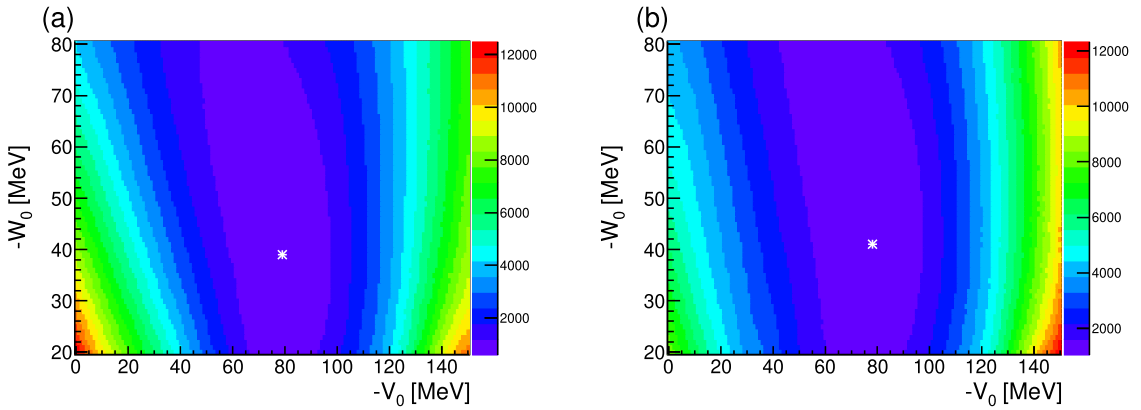

Fig. 16. Two dimensional χ^2 plots as functions of the V_0 and W_0 parameters. The white asterisk shows the parameter set giving the minimum χ^2. (a) Two-dimensional χ^2 distribution without Breit–Wigner function. In this fit, we choose the fitting region $40 > B_K > -300$ MeV to exclude the event excess region. (b) Two-dimensional χ^2 distribution with a Breit–Wigner function. In this fit, the fitting region is $300 > B_K > -300$ MeV.

absorptions, as in Fig. 14, the peak position and decay width are changed by ∼10 MeV and ∼5 MeV, respectively. The production cross section is also affected by the assumption of the branching ratio. When we assume the extreme absorption ratio of (1N : 2N) = (0% : 100 %), the evaluated cross section changes to 50 μb/sr.

What is a possible interpretation of the Breit–Wigner component? As described, we have a quasi-bound state of the kaonic nucleus in the calculation. A possible interpretation is a bound state between a Y^* and residual nucleus, called the Y^*-nucleus. Here, Y^* should be $\Lambda(1405)$ or $\Sigma(1385)$ because the Y^* mass should be smaller than the $\bar{K}N$ threshold. A bound state of Λ- or Σ-hypernuclei is difficult to conjecture because the energy region is quite different.

Figure 17 illustrates a schematic view of the excitation energy spectrum depending on the potentials. The green dashed line shows a schematic spectrum without any secondary interaction, and the black line shows an expected spectrum due to $U_{\bar{K}}$. Because of the strong attraction of the real potential $V_{\bar{K}}$, the peak position of the quasi-elastic process should be shifted to the lower mass side. The red hatched area shows the imaginary part component W_K. Because of the absorptive imaginary potentials, the peak height of the quasi-free reaction should be suppressed.

The orange filled area shows a component of the quasi bound-state of the Y^* nucleus in the deeply bound region. As shown in Fig. 17, we suppose that the Y^* production via the $\bar{K}N$ absorption, K^-"p" $\rightarrow K^- p_{(\mathrm{measured})}$, $K^- N \rightarrow Y^*$ significantly influences the production of the Y^* nucleus. This means that the Y^*-nucleus will be produced because of the strong attractive potential, V_{Y^*}, between the Y^* via the $\bar{K}N$ absorption and residual nucleus. Here, $p_{(\mathrm{measured})}$ is the proton measured by our spectrometer. A similar discussion was also given for the production of a neutron-rich Λ hypernucleus ${}^{6}_{\Lambda}\mathrm{H}$ via the ${}^{6}\mathrm{Li}(\pi^-, K^+)$ reaction (J-PARC E10 experiment) [58,59]. It was discussed that a Σ-doorway reaction such as π^-"p" $\rightarrow \Sigma^- K^+$, Σ^-"p" $\rightarrow \Lambda n$, is significant for the ${}^{6}_{\Lambda}\mathrm{H}$ production. The ${}^{6}_{\Lambda}\mathrm{H}$ should theoretically be produced because of the attractive potential, V_Λ, between Λ via the $\Sigma N \rightarrow \Lambda N$ absorption and residual nucleus.

The concept of the $\Lambda(1405)$-nucleus was discussed in Refs. [60,61]. A clear signal of $\Lambda(1405)$ was observed in the $\pi^\pm\Sigma^\mp$ invariant-mass spectra of the ${}^{3}\mathrm{He}(K^-, \pi^\pm\Sigma^\mp p)n$ reaction by J-PARC E15 [62]. Therefore, $\Lambda(1405)$ should be produced via the reaction process of K^-"p"

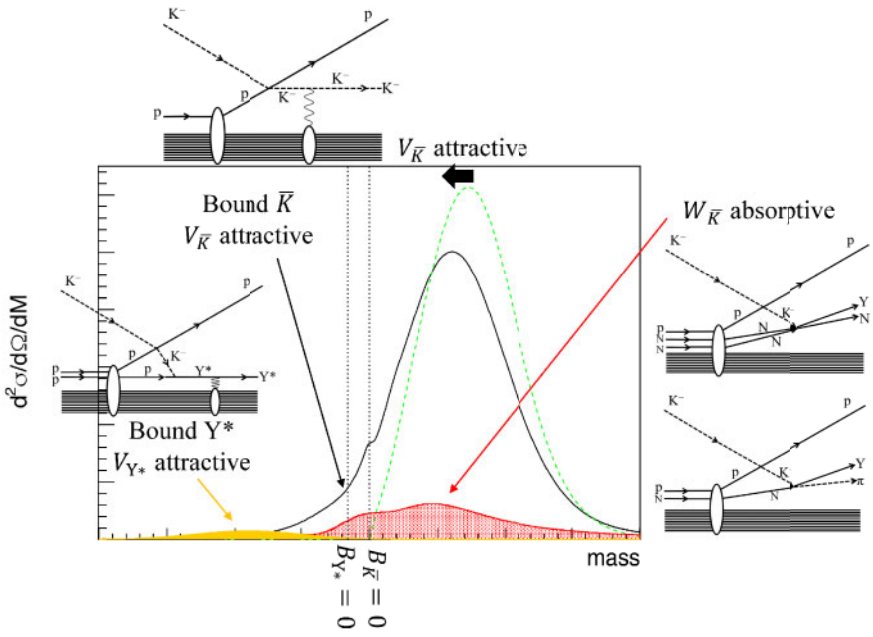

Fig. 17. Schematic view of the excitation energy spectrum depending on the potential for the $^{12}C(K^-,p)$ reaction. A green dashed line shows the schematic spectrum without any secondary interaction. The black line shows the expected spectrum due to $U_{\bar{K}}$. The component caused by the imaginary part $W_{\bar{K}}$ is shown by a red hatched area. The red hatched area shows the component of the quasi-bound state of a Y^* nucleus in the deeply bound region because of the attractive real potentials of V_{Y*}, shown by a orange filled area.

$\rightarrow K^- p_{(\text{measured})}$, $K^- N \rightarrow \Lambda(1405)$. There might also exist a $\Sigma(1385)$-nucleus because there should be an attraction in the interaction between a decuplet baryon and nucleon [63]. Moreover, the "Y^* shift" observed in the inclusive $d(\pi^+,K^+)$ spectrum by J-PARC E27 could be a hint of a Y^*-nucleus state [64].

Next, we discuss the relationship between the interpretation of the Y^*-nucleus and the study of kaonic-atom X-rays (see Sect. 1). In Ref. [23], Friedman and Gal produced the single $\bar{K}$–nucleon potential $V_{\bar{K}}^{(1)}$ based on the chiral unitary model. In addition, they considered a phenomenological potential $V_{\bar{K}}^{(2)}$, which corresponds to the potential for the two- (multi-)nucleon absorption process, to explain the kaonic-atom X-ray data. The evaluated potential depths of $V_{\bar{K}}^{(1)}$ and $V_{\bar{K}}^{(2)}$ in this theoretical analysis are -60 MeV and -140 MeV, respectively. In other words, the deep real potential ($V_{0\bar{K}}^{(2)} = -140$ MeV) is obtained for the two- (multi-)nucleon absorption process in Ref. [23]. Here, we can conjecture that the Y^* doorway process, K^-"p" $\rightarrow Y^*$, Y^*"N" $\rightarrow YN$ is a key process to derive the deep real potential for the two- (multi-)nucleon absorption in the stopped K^- reaction. This means that the strong attractive Y^*-nucleus potential, V_{Y*}, may be a basis for deriving the deep $V_{\bar{K}}^{(2)}$ potential. Note that the Y^*-nucleus potential, V_{Y*}, cannot contribute to the single $\bar{K}$–nucleon potential $V_{\bar{K}}^{(1)}$.

Finally, we mention the coincidence spectrum obtained by using the decay counter, KIC. Figure 18(a) shows a comparison between the inclusive and coincidence spectra, shown respectively by black and green lines. We request at least one charged particle hit in the up or down segments for the coincidence spectrum, which is the same requirement as in KEK E548 [26]. We check the distortion effect because of the coincidence requirement by evaluating the coincidence

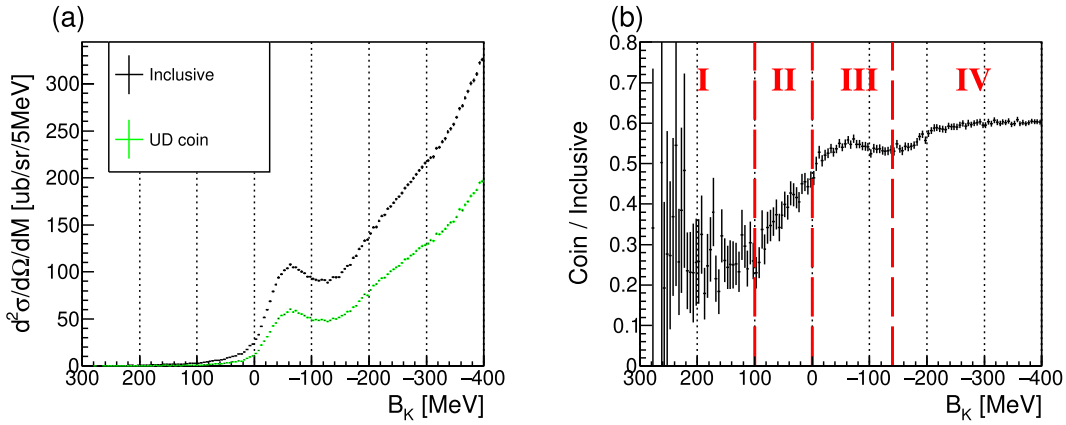

Fig. 18. (a) Comparison between the inclusive and coincidence spectra shown by black and green points, respectively. (b) Coincidence probability spectrum calculated by dividing the coincidence spectrum by the inclusive spectrum.

probability spectrum (Fig. 18(b)). The coincidence probability spectrum is calculated by dividing the coincidence spectrum (green points) by the inclusive spectrum (black points).

If there is no distortion, the coincidence probability spectrum should be flatly distributed. However, we notice that the coincidence probability is significantly different in the four regions identified by I, II, III, and IV in the figure. In region IV, the coincidence probability gradually changes from $B_K = -200$ MeV to -150 MeV, whereas the probability is almost flat at $B_K < -210$ MeV. It can be understood because the production threshold of $\bar{K}\pi N$ opens at $B_K \sim -140$ MeV. In region III, the coincidence probability is almost flat because the dominant process is the $K^- p$ quasi-elastic reaction in this region.

The probability drastically changes in region II and is flat in region I, with the lowest value of Coin/Inclusive ~ 0.25. The observed trend could help to deepen our understanding of the Y^*-nucleus state. We have a plan to measure the exclusive spectra in the near future (Sect. 7) and it will allow us to clarify our interpretation.

7. Summary and outlook

We have measured the inclusive spectrum without any triggered bias of the $^{12}\mathrm{C}(K^-, p)$ reaction with high statistics and high energy resolution for the first time. We have derived the optical potential between the $\bar{K}$ and a nucleus by comparing the measured spectrum with the theoretical calculation by varying both the real and imaginary parts. Then, we found that the measured spectrum is reproduced reasonably well when we choose the real part of the potential as -80 MeV, corresponding to the "shallow" potential predicted by the chiral models.

However, there is a significant excess of the yield in the deeply bound region of $B_K \sim 100$ MeV. This event excess cannot be reproduced by any $\bar{K}$–nucleus potential parameters or background process. The enhancement is fitted well by a Breit–Wigner function at an energy of $B_K = 90$ MeV and a width of 100 MeV. In this model, the possible contribution of Y^* production via the K^- absorption process is not explicitly considered in the real part of the $\bar{K}$–nucleus potential. Then, the Breit–Wigner component can be interpreted as a bound Y^*-nucleus state.

We did not observe a clear signal of the kaonic-nucleus or Y^*-nucleus state as a distinct peak in the inclusive spectrum. To observe it as a distinct peak, we need exclusive spectra obtained by measuring

decay particles in coincidence. At J-PARC, the E42 experiment is planned [65] to search for the H-dibaryon. The E42 experiment will also use the same reaction as the present experiment (E05), namely $^{12}\mathrm{C}(K^-, K^+)$ at 1.8 GeV/c. Here, we can measure the $^{12}\mathrm{C}(K^-, p)$ spectrum simultaneously under the same conditions as the E05 experiment. In the case of E42, a large acceptance time projection chamber, called HypTPC, will be used to measure the decay particles. It will allow us to measure the exclusive spectra, clarifying our interpretation. It is presumed that the kaonic-nucleus and Y^*-nucleus states will be distinguished by measuring their mesonic and non-mesonic decays, respectively. Moreover, it will be interesting to conduct the same inclusive analysis by changing the target mass number to study the A dependence of the $\bar{K}A$ potential.

Acknowledgements

We would like to thank the Hadron beam channel group, the accelerator group, and the cryogenics section at J-PARC for their great efforts on stable machine operation and beam quality improvements. The authors acknowledge the support of NII for SINET4. We are also grateful for the fruitful discussions with Prof. T. Yamazaki, Prof. Y. Akaishi, and Dr. T. Sekihara. The work was supported by Japan Society for the Promotion of Science (JSPS) KAKENHI Grant Numbers JP16K05355, JP18K13545, and 18H05403. The authors would like to thank Enago (https://www.enago.jp) for the English language review.

Appendix A. Differential cross section of K^-p elastic scattering at $p_K = 1.8$ GeV/c

Table A.1 summarizes the measured differential cross section of the $K^-p \to K^-p$ elastic scattering at $p_K = 1.8$ GeV/c. We show two types of errors, namely the statistical error and the systematic error, evaluated by considering the uncertainty of the efficiency.

Table A.1. Summary of measured differential cross section of the K^-p elastic scattering. The values are also shown in Fig. 10.

$\theta_{Kp(\mathrm{Lab})}$ [degree]	$d\sigma/d\Omega$ [μb/sr]
0.5–1.5	381.3 ± 19.9 (stat.) ± 13.5 (syst.)
1.5–2.5	433.2 ± 21.7 (stat.) ± 15.4 (syst.)
2.5–3.5	463.4 ± 22.1 (stat.) ± 16.4 (syst.)
3.5–4.5	507.4 ± 23.3 (stat.) ± 18.0 (syst.)
4.5–5.5	531.8 ± 23.8 (stat.) ± 18.9 (syst.)
5.5–6.5	608.1 ± 25.5 (stat.) ± 21.6 (syst.)
6.5–7.5	740.5 ± 28.0 (stat.) ± 26.3 (syst.)
7.5–8.5	870.0 ± 30.6 (stat.) $^{+30.9}_{-31.0}$ (syst.)
8.5–9.5	947.3 ± 32.1 (stat.) ± 33.9 (syst.)
9.5–10.5	938.1 ± 31.8 (stat.) $^{+33.5}_{-33.6}$ (syst.)
10.5–11.5	846.8 ± 30.6 (stat.) $^{+30.2}_{-30.3}$ (syst.)
11.5–12.5	706.9 ± 28.1 (stat.) $^{+25.2}_{-25.3}$ (syst.)
12.5–13.5	555.0 ± 25.1 (stat.) $^{+19.9}_{-20.0}$ (syst.)
13.5–14.5	483.4 ± 23.6 (stat.) $^{+17.3}_{-17.5}$ (syst.)
14.5–15.5	383.2 ± 21.0 (stat.) $^{+13.7}_{-13.9}$ (syst.)
15.5–16.5	359.9 ± 20.1 (stat.) $^{+12.9}_{-13.1}$ (syst.)
16.5–17.5	331.7 ± 19.6 (stat.) $^{+14.8}_{-18.6}$ (syst.)
17.5–18.5	320.3 ± 19.2 (stat.) $^{+14.3}_{-18.0}$ (syst.)
18.5–19.5	290.9 ± 18.4 (stat.) $^{+24.9}_{-49.8}$ (syst.)
19.5–20.5	263.8 ± 18.2 (stat.) $^{+22.6}_{-45.1}$ (syst.)

Appendix B. Detailed comparison with different $\bar{K}A$ potential

A detailed comparison between the obtained $^{12}\mathrm{C}(K^-,p)$ spectrum and the template fit with various $\bar{K}A$ potentials is shown below. Figure B.1 shows the dependence on the real part depth, V_0, with a fixed imaginary part depth, W_0. On the other hand, the imaginary part, W_0, has a weak effect on the $^{12}\mathrm{C}(K^-,p)$ spectrum (Fig. B.2). The best fit is obtained using the optical potential $(V_0, W_0) = (-80, -40)$ MeV. Note that the significant excess of the yield in the deeply bound region $B_K \sim 100$ MeV cannot be reproduced by any potential values in this theoretical work.

Appendix C. The calculated spectrum with the optimum potential parameters

Figure C.1 shows the calculated spectrum with the optimum optical potential $(V_0, W_0) = (-80, -40)$ MeV without introducing the experimental smearing of the energy resolution. The black line displays the total spectrum. The solid lines in different colors show each subcomponent of the nucleon hole state. As shown by the red line, the K^- quasi-bound state corresponding to the kaon s-state coupled with the proton hole of the $1p_{3/2}$ state exists at $B_K = 31$ MeV and $\Gamma = 53$ MeV.

On the other hand, the kaon p-state coupled with the proton hole $1p_{3/2}$ state, displayed by a green line, is unbound and enhances near the threshold energy. However, this enhancement is smeared out when the experimental resolution of 4.2 MeV is considered. Note that the main component of the bound region in the calculated spectrum is not a scattering state with the absorption process caused by the imaginary part of the potential, but a nuclear bound state (real part of the potential), while we cannot see it as a distinct peak because of its large decay width. The contribution of the kaonic bound state is estimated to be ∼2% of the quasi-elastic component in our theoretical model.

Appendix D. Examination of the background processes to explain the event excess

We examine two types of background reactions to explain the observed event excess in the deeply bound region $B_K \sim 100$ MeV:

D1: One-step two-nucleon absorption process:
K^-"NN" $\to Yp_{(\mathrm{measured})}$.
D2: Two-step three-nucleon absorption process:
K^-"N" $\to K^-N$, K^-"NN" $\to Yp_{(\mathrm{measured})}$.

Here, the "NN" shows two nucleons inside the ^{12}C target, Y corresponds to the Λ or Σ particle, and $p_{(\mathrm{measured})}$ means the measured proton, which is emitted to the forward angle by our spectrometer. We discuss the possibility for each case below.

D1: One-step two-nucleon absorption: K^-"NN" $\to Yp_{(\mathrm{measured})}$

The proton emitted from the one-step two-nucleon absorption K^-"NN" $\to Yp$ can have a high momentum. Figure D.1 shows the simulated missing-mass spectra of these one-step two-nucleon absorption processes. In this simulation, the spectra are smeared by the nucleon Fermi motion in the ^{12}C target, and the forward-scattering angle range ($3.5° < \theta_p < 4.5°$) is selected. Each reaction process is displayed by lines with different colors.

As shown by black and green spectra, these processes are broad bump structures. These peak positions correspond to $B_K \sim 210$ MeV (K^-"NN" $\to \Lambda p_{(\mathrm{measured})}$) and $B_K \sim 150$ MeV (K^-"NN" $\to \Sigma p_{(\mathrm{measured})}$). These yields, especially for K^-"NN" $\to \Lambda p_{(\mathrm{measured})}$, concentrate in a much deeper B_K region compared to the observed event excess shown in Figs. B.1 and B.2. We also

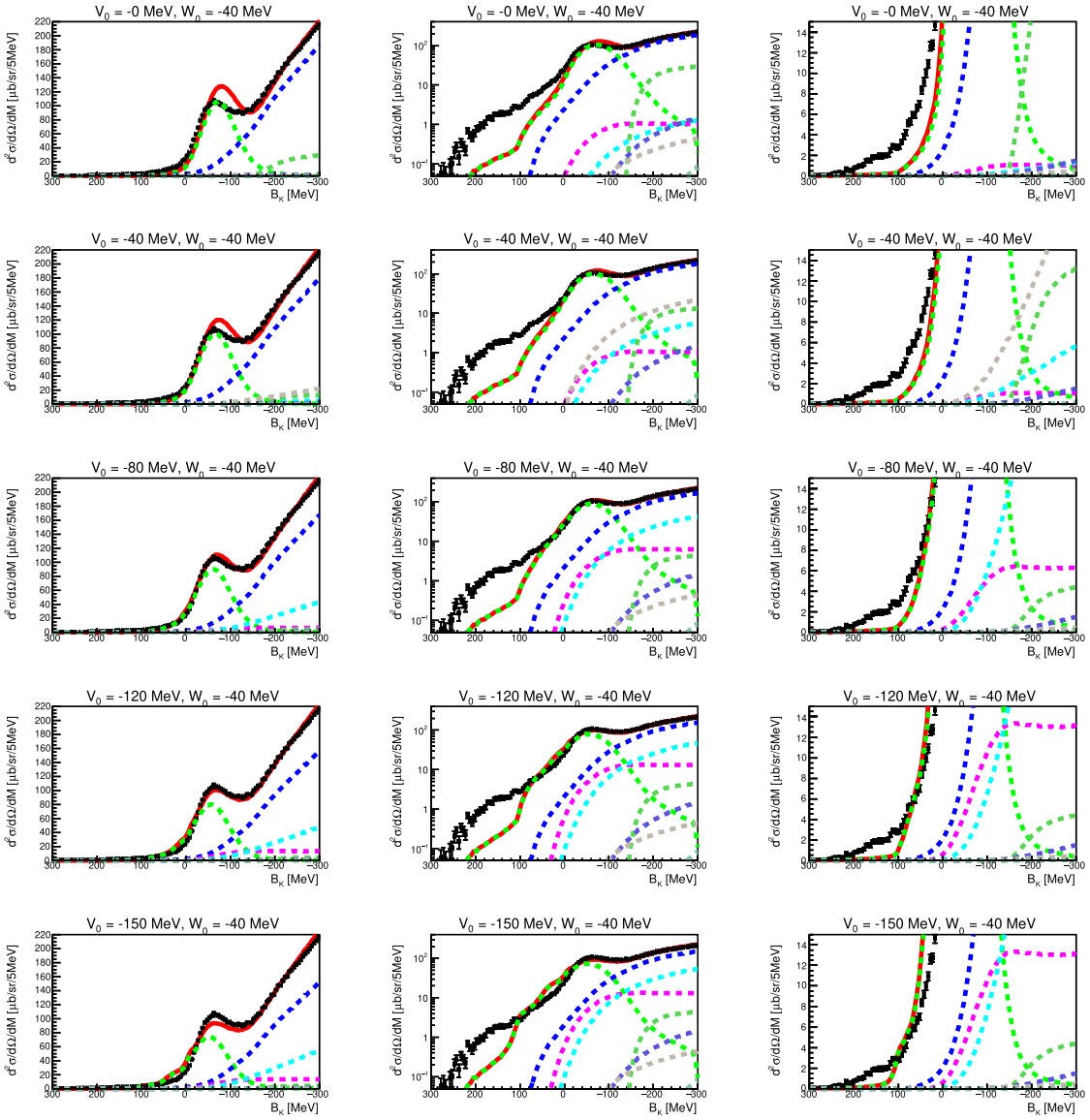

Fig. B.1. Detailed comparison between the data and the template fit with various V_0 values. The imaginary part is fixed to the optimum value $W_0 = -40$ MeV. The title of each plot shows the V_0 values. The green dotted lines show the theoretical calculations for the $K^- p$ quasi-elastic process obtained by the Green's function method. The other colored dotted lines show the calculated spectral shapes for the background processes (see Fig. 11). The total fit results are displayed by red lines. The left and middle columns show the same spectra with linear and semi-log scales, respectively, and the right column shows the magnified view for a small cross section region.

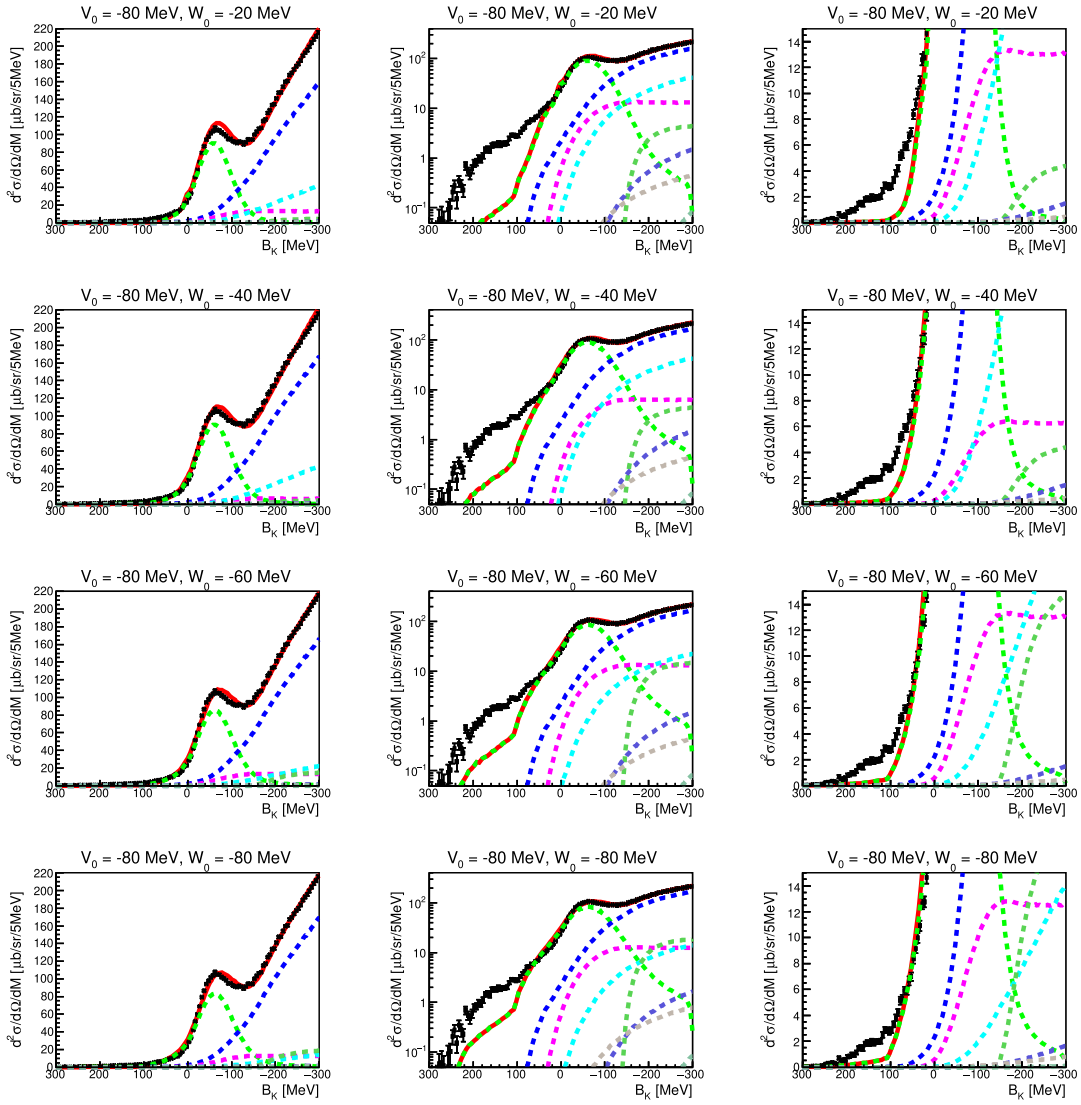

Fig. B.2. Detailed comparison between the data and the template fit with various W_0 values. The real part is fixed to the optimum value $V_0 = -80$ MeV. The title of each plot shows the W_0 values. The green dotted lines show the theoretical calculations for the $K^- p$ quasi-elastic process obtained by the Green's function method. The other colored dotted lines show the calculated spectral shapes for the background processes (see Fig. 11). The red lines display the total fit results. The left and middle columns show the same spectra with linear and semi-log scales, respectively, and the right column shows the magnified view for a small cross section region.

consider the protons originating from the hyperon decay K^-"NN" $\to Yp$, $Y \to p_{(\text{measured})}\pi(\gamma)$, as shown by red, blue, and magenta lines. These distributions are almost flat, and it is difficult to reproduce the measured event excess.

Figure D.2 shows the template fit result by adding the one-step two-nucleon absorption processes instead of the Breit–Wigner component of Fig. 15. The gray and green hatched spectra display the components of K^-"NN" $\to \Lambda p$ and K^-"NN" $\to \Sigma p$, respectively. In this fit, each yield is a free parameter. As shown in this figure, the measured enhancement in the region $200 \gtrsim B_K \gtrsim 80$ MeV is difficult to reproduce by these one-step two-nucleon absorption processes. We expect that the cross

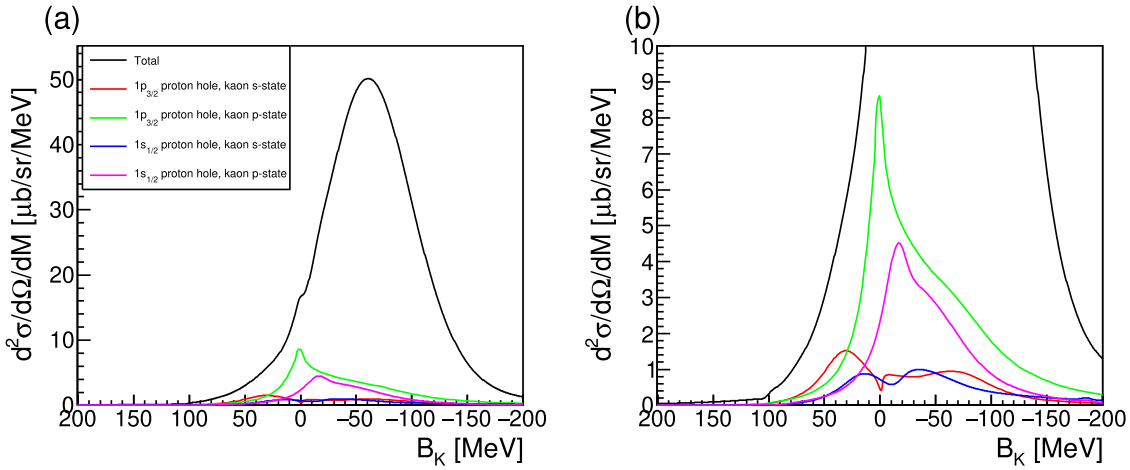

Fig. C.1. (a) Theoretical calculation with the optimum potential $(V_0, W_0) = (-80, -40)$ MeV. The black line displays the total spectrum. The solid lines in different colors show the subcomponents of the different proton holes, $1s_{1/2}$ or $1p_{3/2}$, and kaonic orbital states, s or p. (b) Magnified view of (a) to see the small cross section region.

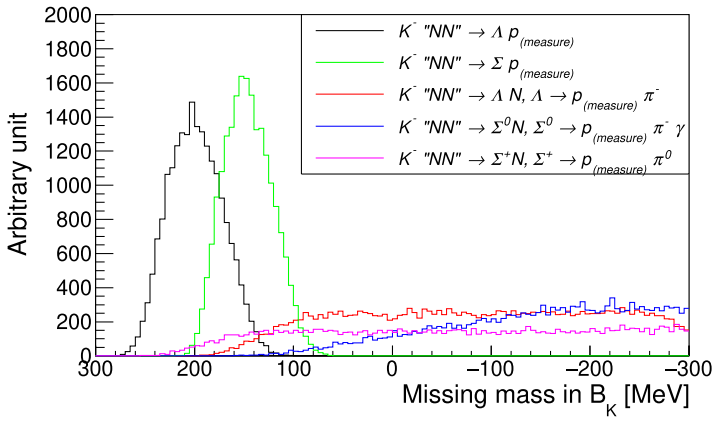

Fig. D.1. Simulated missing-mass spectra of the $^{12}C(K^-, p)$ reaction for one-step two-nucleon absorption processes plotted in the scale of B_K; $p_{(\mathrm{measured})}$ is the proton measured by our spectrometer.

section of these one-step two-nucleon absorption processes should be small because the incident K^- beam momentum of 1.8 GeV/c is much higher than the nucleon Fermi motion in ^{12}C.

D2: Two-step three-nucleon absorption: K^-"N" $\to K^-N$, K^-"NN" $\to Yp_{(\mathrm{measured})}$

We discuss the possibility of the two-step three-nucleon absorption processes K^-"N" $\to K^-N$, K^-"NN" $\to Yp_{(\mathrm{measured})}$. In this reaction, the scattered K^- at the first step is absorbed by two nucleons, and a Yp pair is produced via absorption. Figure D.3 shows the simulated correlation plots between the binding energy (B_K) and K^- recoil momentum at the first-step reaction. The black (green) boxes in Fig. D.3(a) show the case of K^-"N" $\to K^-N$, K^-"NN" $\to \Lambda p_{(\mathrm{measured})}(\Sigma p_{(\mathrm{measured})})$. Also, the magenta boxes in this figure show the correlation of the two-step two nucleon absorption process of K^-"N" $\to K^-N$, K^-"p" $\to K^- p_{(\mathrm{measured})}$. We also evaluate the case in which the measured proton is produced from the hyperon decay K^-"N" $\to K^-N$, K^-"NN" $\to Yp, Y \to p_{(\mathrm{measured})}\pi$. These spectra are displayed by red and blue boxes in Fig. D.3(b), where Y is Λ and Σ, respectively.

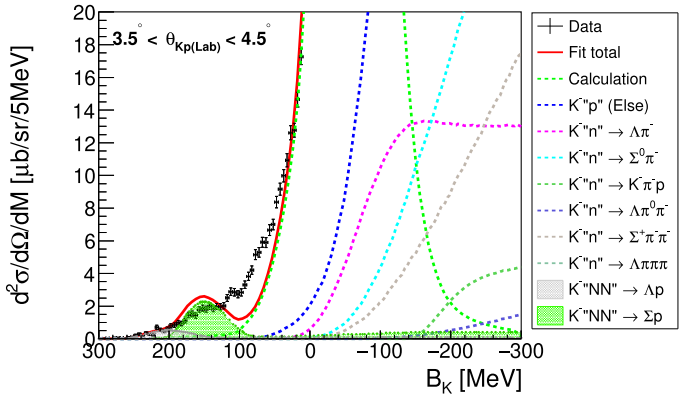

Fig. D.2. (a) The magnified view of the small cross section of the template fit result by adding the one-step two-nucleon absorption processes. The components of K^-"NN" $\rightarrow$ Λp and K^-"NN" $\rightarrow$ Σp are displayed by gray and green hatched spectra, respectively. The green dotted line shows the calculated spectrum with the optical potential of $(V_0, W_0) = (-80, -40)$ MeV. The other color assignments are the same as in Fig. 11.

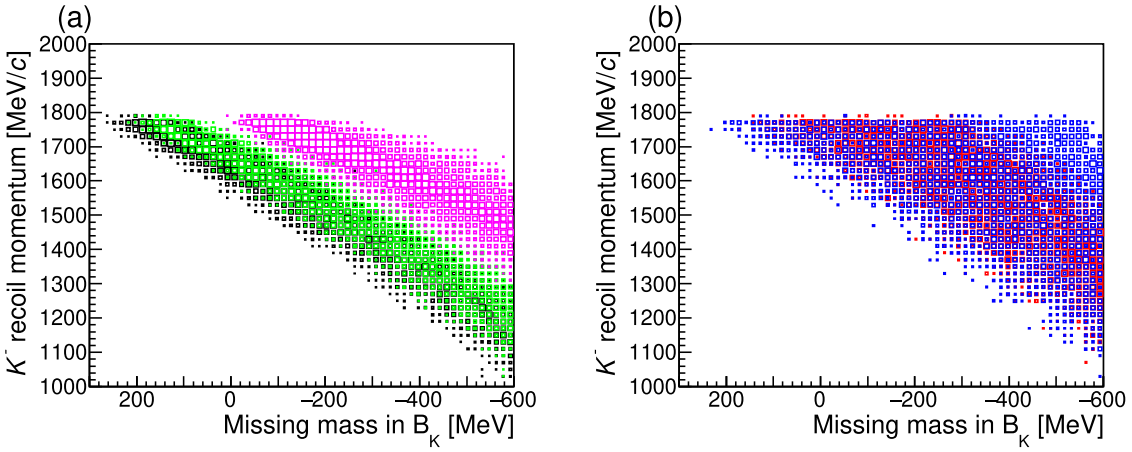

Fig. D.3. Simulated correlations between the binding energy of the B_K and K^- recoil momentum of the two-step three-nucleon absorption processes. See details in the text.

We notice that these two-step three-nucleon absorption processes kinematically exist in the deeply bound region ($B_K = 100 \sim 200$ MeV), as shown by the black, green, red, and blue spectra, while the two-step two-nucleon absorption process does not, as indicated by the magenta distribution. However, the K^- recoil momentum should be $\sim$1.8 GeV/c, as high as the incident beam momentum, to reach the deeply bound region. Moreover, the two-nucleon absorption reaction at the second step, K^-"NN" $\rightarrow$ $Yp_{(\mathrm{measured})}$, is the same reaction as in process D1. Since we cannot isolate the signal of the absorption reaction D1, Its cross section should be very small. Therefore, the cross section of the two-step three-nucleon absorption processes should be much smaller. The sticking probability is inversely proportional to the square of the recoil momentum. Consequently, we conjecture that it is difficult to ascribe the origin of the event excess to these two-step three-nucleon absorption processes.

References

[1] T. Kishimoto, Phys. Rev. Lett. **83**, 4701 (1999).
[2] Y. Akaishi and T. Yamazaki, Phys. Rev. C **65**, 044005 (2002).

[3] A. Gal, Nucl. Phys. A **914**, 270 (2013).
[4] R. Aaij et al. [LHCb Collaboration], Phys. Rev. Lett. **115**, 072001 (2015).
[5] R. Aaij et al. [LHCb Collaboration], Phys. Rev. Lett. **122**, 222001 (2019).
[6] R. H. Dalitz, Eur. Phys. J. C **15**, 748 (2000).
[7] T. Hyodo and D. Jido, Prog. Part. Nucl. Phys. **67**, 55 (2012).
[8] J. M. M. Hall, W. Kamleh, D. B. Leinweber, B. J. Menadue, B. J. Owen, A. W. Thomas, and R. D. Young, Phys. Rev. Lett. **114**, 132002 (2015).
[9] M. Agnello et al. [FINUDA Collaboration], Phys. Rev. Lett. **94**, 212303 (2005).
[10] T. Yamazaki et al., Phys. Rev. Lett. **104**, 132502 (2010).
[11] G. Agakishiev et al., Phys. Lett. B **742**, 242 (2015).
[12] A. O. Tokiyasu et al. [LEPS Collaboration], Phys. Lett. B **728**, 616 (2014).
[13] Y. Ichikawa et al., Prog. Theor. Exp. Phys. **2015**, 021D01 (2015).
[14] S. Ajimura et al. [J-PARC E15 Collaboration], Phys. Lett. B **789**, 620 (2019).
[15] M. Bazzi et al. [SIDDHARTA Collaboration], Phys. Lett. B **704**, 113 (2011).
[16] C. J. Batty, E. Friedman, and A. Gal, Phys. Rept. **287**, 385 (1997).
[17] T. Wass, N. Kaiser, and W. Weise, Phys. Lett. B **365**, 12 (1996).
[18] M. Lutz, Phys. Lett. B **426**, 12 (1998).
[19] A. Ramos and E. Oset, Nucl. Phys. A **671**, 481 (2000).
[20] A. Cieplý, E. Friedman, A. Gal, and J. Mareš, Nucl. Phys. **696**, 173 (2001).
[21] J. Mareš, E. Friedman, and A. Gal, Nucl. Phys. A **770**, 84 (2006).
[22] N. Barnea and E. Friedman, Phys. Rev. C **75**, 022202(R) (2007).
[23] E. Friedman and A. Gal, Nucl. Phys. A **899**, 60 (2013).
[24] Y. Ikeda, T. Hyodo, and W. Weise, Phys. Lett. B **706**, 63 (2011).
[25] C. Vander Velde-Wilquet, J. Sacton, J. H. Wickens, D. N. Tovee, and D. H. Davis, Nuovo Cim. A **39**, 538 (1977).
[26] T. Kishimoto et al., Prog. Theor. Phys **118**, 181 (2007).
[27] V. K. Magas, J. Yamagata-Sekihara, S. Hirenzaki, E. Oset, and A. Ramos, Phys. Rev. C **81**, 024609 (2010).
[28] T. Takahashi et al., Prog. Theor. Exp. Phys. **2012**, 02B010 (2012).
[29] T. O. Yamamoto et al. [J-PARC E13 Collaboration], Phys. Rev. Lett. **115**, 222501 (2015).
[30] R. Honda, K. Miwa, Y. Matsumoto, N. Chiga, S. Hasegawa, and K. Imai, Nucl. Instr. Meth. A **787**, 157 (2015).
[31] M. Moritsu et al. [J-PARC E19 Collaboration], Phys. Rev. C **90**, 035205 (2014).
[32] R. Honda et al. [J-PARC E10 Collaboration], Phys. Rev. C **96**, 014005 (2017).
[33] J. Myrheim and L. Bugge, Nucl. Instr. Meth. **160**, 43 (1979).
[34] A. de Bellefon et al., Nuovo Cim. A **7**, 567 (1972).
[35] A. Berthon et al., Nuovo Cim. A **21**, 146 (1974).
[36] A. Berthon, L. K. Rangan, J. Vrana, I. Butterworth, P. J. Litchfield, A. M. Segar, J. R. Smith, J. Meyer, E. Pauli, and B. Tallini, Nucl. Phys. B **20**, 476 (1970).
[37] A. Berthon, J. Vrana, I. Butterworth, P. J. Litchfield, J. R. Smith, J. Meyer, E. Pauli, and B. Tallini, Nucl. Phys. B **24**, 417 (1970).
[38] P. J. Litchfield, R. J. Hemingway, P. Baillon, A. Albrecht, and A. Putzer, Nucl. Phys. B **74**, 39 (1974).
[39] P. J. Litchfield, R. J. Hemingway, P. Baillon, A. Putzer, and H. Schleich, Nucl. Phys. B **74**, 19 (1974).
[40] P. J. Litchfield, R. J. Hemingway, P. Baillon, H. Albrecht, and E. Burkhardt, Nucl. Phys. B **74**, 12 (1974).
[41] A. Brandstetter, I. Butterworth, S. M. Deen, P. J. Litchfield, A. Berthon, J. Vrana, J. Zatz, W. Wojcik, J. Meyer, and B. Tallini, Nucl. Phys. B **39**, 13 (1972).
[42] W. Cameron et al. [Rutherford Laboratory-Imperial College Collaboration], Nucl. Phys. B **146**, 327 (1978).
[43] W. Cameron et al. [Rutherford Laboratory-Imperial College Collaboration], Nucl. Phys. B **143**, 189 (1978).
[44] P. J. Litchfield et al., Nucl. Phys. B **30**, 125 (1971).
[45] P. C. Barber et al., Nucl. Phys. B **102**, 365 (1976).
[46] R. J. Hemingway, J. Eades, D. M. Harmsen, J. O. Petersen, A. Putzer, C. Kiesling, D. E. Plane, and W. Wittek, Nucl. Phys. B **91**, 12 (1975).

[47] K. Abe, B. A. Barnett, J. H. Goldman, A. T. Laasanen, P. H. Steinberg, G. J. Marmer, D. R. Moffett, and E. F. Parker, Phys. Rev. D **12**, 6 (1975).
[48] J. Yamagata, H. Nagahiro, and S. Hirenzaki, Phys. Rev. C **74**, 014604 (2006).
[49] N. Ikeno, H. Nagahiro, and S. Hirenzaki, Eur. Phys. J. A **47**, 161 (2011).
[50] C. W. De Jager, H. De Vries, and C. De Vries, Atom. Data Nucl. Data Tabl. **14**, 479 (1974); **16**, 580 (1975) [erratum].
[51] O. Morimatsu and K. Yazaki, Nucl. Phys. A **435**, 727 (1985).
[52] O. Morimatsu and K. Yazaki, Nucl. Phys. A **483**, 493 (1988).
[53] J. Yamagata, H. Nagahiro, Y. Okumura, and S. Hirenzaki, Prog. Theor. Phys. **114**, 301 (2005); **114**, 905 (2005) [erratum].
[54] O. Morimatsu and K. Yazaki, Prog. Part. Nucl. Phys. **33**, 679 (1994).
[55] J. Nieves, E. Oset, and C. Garcia-Recio, Nucl. Phys. A **554**, 509 (1993).
[56] T. Hashimoto et al. [J-PARC E15 Collaboration], Prog. Theor. Exp. Phys. **2015**, 061D01 (2015).
[57] J. Yamagata and S. Hirenzaki, Eur. Phys. J. A **31**, 255 (2007).
[58] T. Harada, R. Honda, and Y. Hirabayashi, Phys. Rev. C **97**, 024601 (2018).
[59] T. Harada and Y. Hirabayashi, Phys. Rev. C **95**, 044610 (2017).
[60] A. Arai, M. Oka, and S. Yasui, Prog. Theor. Phys. **119**, 103 (2008).
[61] T. Uchino, T. Hyodo, and M. Oka, Nucl. Phys. A **868–869**, 53 (2011).
[62] H. Ohnishi, F. Sakuma, and T. Takahashi, Prog. Part. Nucl. Phys. **113**, 103773 (2020).
[63] H. Garcilazo and A. Gal, Nucl. Phys. A **897**, 167 (2013).
[64] Y. Ichikawa et al., Prog. Theor. Exp. Phys. **2014**, 101D03 (2014).
[65] J. K. Ahn et al., J-PARC E42 proposal (available at: http://j-parc.jp/researcher/Hadron/en/pac_1201/pdf/KEK_J-PARC-PAC2011-06.pdf, date last accessed September 19, 2020).